PHYSICAL REVIEW B VOLUME 43, NUMBER 18 15 JUNE 1991-II

Mechanism of low-temperature ($\leq 300\,^{\circ}\mathrm{C}$) crystallization and amorphization for the amorphous Si layer on the crystalline Si substrate by high-energy heavy-ion beam irradiation

J. Nakata
NTT LSI Laboratories, 3-1, Morinosato Wakamiya, Atsugi-shi, Kanagawa Pref., 243-01, Japan
(Received 10 September 1990)

By high-energy ($\sim$2.5-MeV) heavy-ion ($^{75}\mathrm{As}^+$, $^{84}\mathrm{Kr}^+$, $^{131,132}\mathrm{Xe}^+$, etc.) beam irradiation, the amorphous Si layers on the crystalline Si substrates formed by low-energy ($\sim$100-keV) ion implantation or by chemical-vapor deposition could be crystallized epitaxially at very low substrate temperatures (120–300 °C, in the 2.5-MeV $^{75}\mathrm{As}^+$ irradiation case), far below the ordinary solid-phase ($\sim$600 °C) or liquid-phase ($\sim$1400 °C) epitaxial growth temperatures. Layer-by-layer amorphization of amorphous Si layers on the crystalline Si substrates also occurred at low temperatures ($\leq$120 °C, in the 2.5-MeV $^{75}\mathrm{As}^+$ irradiation case). The author elucidates the low-temperature (120–300 °C) crystallization mechanism and the low-temperature ($\leq$120 °C) amorphization mechanism. The thermal diffusion of vacancies towards the amorphous layer, produced by nuclear scattering of incident heavy ions in the crystalline substrate, plays an important role in the low-temperature crystallization. High incident energies also contribute to the enhanced vacancy diffusion due to their large electronic scattering. Whether crystallization or amorphization occurs depends on the balance at the crystalline-amorphous interface, between the vacancy concentration supplied from the crystalline substrate toward the amorphous layer via thermal diffusion and the interstitial Si-atom concentration supplied from the amorphous layer toward the crystalline substrate via recoil by incident heavy ions.

I. INTRODUCTION

Various annealing methods, such as furnace, laser (pulsed or cw),[1] electron-beam (pulsed or cw),[2] and ion-beam (pulsed or cw)[3–10] annealing methods, have been used to crystallize amorphous Si layers on crystalline Si substrates, or to activate dopant atoms in the amorphous or damaged regions in the crystalline substrate. In these annealing methods, except Refs. 4–10, the amorphous layers or the damaged regions were heated up to the solid-phase epitaxial growth (SPEG) temperature of $\sim$600 °C or to the liquid-phase epitaxial growth (LPEG) temperature of $\sim$1400 °C.

The author reported previously[11,12] that the amorphous Si layers could be crystallized below the $\sim$300 °C substrate temperatures by high-energy ($\sim$2.5-MeV) heavy-ion ($^{75}\mathrm{As}^+$, $^{84}\mathrm{Kr}^+$, $^{131,132}\mathrm{Xe}^+$, etc.) beam irradiation. Additionally, it was emphasized that even just under the irradiation beam spot on the surface of a Si wafer, the substrate temperatures had been kept below $\sim$300 °C, far below the ordinary SPEG temperature. In these articles, the author also reported that greater amorphization, that is, layer-by-layer amorphization of the amorphous Si layer, occurred below the 120 °C substrate temperatures in the 2.5-MeV $^{75}\mathrm{As}^+$ irradiation case. It was proposed that the vacancies produced by incident heavy ions in the crystalline substrate under the amorphous layer migrated toward the amorphous layer via thermal diffusion, and interacted with the amorphous layer at the crystalline-amorphous interface, resulting in crystallization. The author deduced that the doubly negative vacancies produced by the large electronic scattering of high-energy incident ions enhanced the migration velocity due to their low activation energy of $\sim$0.2 eV for migration. However, the exact mechanism of crystallization was not necessarily clear, and the layer-by-layer amorphization mechanism at low temperature was not entirely resolved.

Since then, many experiments have been done on the low-temperature crystallization of amorphous Si layers by ion-beam irradiation, including low-energy (from several tens of kilo-electron volts to several hundred kilo-electron volts energy) and light-ion ($^{4}\mathrm{He}^+$, $^{20}\mathrm{Ne}^+$, $^{40}\mathrm{Ar}^+$, etc.) beam irradiation.

Linnros *et al.*[5,6] confirmed that the amorphous Si layers in silicon on sapphire were epitaxially regrown by irradiation of comparatively light ions, such as $^{4}\mathrm{He}^+$, $^{14}\mathrm{N}^+$, $^{20}\mathrm{Ne}^+$, $^{28}\mathrm{Si}^+$, and $^{40}\mathrm{Ar}^+$ ions with 300-keV energy at the 300 °C substrate temperature. They concluded that the growth rate was proportional to the amount of deposited energy in elastic collisions by the annealing ions near the crystalline-amorphous interface, and did not conspicuously refer to the role of inelastic scattering of annealing ions. They deduced that point-defect migration contributed to the crystallization.

Williams *et al.*[7] also generated epitaxial crystallization of amorphous Si layers on the crystalline Si substrates at 200–450 °C substrate temperatures using 0.6–3.0 MeV $^{20}\mathrm{Ne}^+$ ion irradiation. They concluded that below 400 °C, growth proceeded linearly with a $^{20}\mathrm{Ne}^+$ ion dose and was proportional to nuclear (elastic) energy loss, the same as for the Linnros case.[5,6] They suggested that mobile point defects such as vacancies produced at the near interface were responsible for low-temperature ($\leq$400 °C) crystallization. They also did not refer to the role of the inelastic collision of annealing ions, because the regrowth rate decreased as the incident ion energy in-

 ©1991 The American Physical Society

creased (see Fig. 16).

The amorphization phenomenon, that is, layer-by-layer amorphization of amorphous Si layers on the crystalline Si substrates, pointed out by the author in previous articles,[11,12] was confirmed by Elliman *et al.*[8]

Linnros *et al.*[9] reported that the balance between amorphization and crystallization was controlled by the accumulation of divacancies at the crystalline-amorphous interface. This was because the critical dose rate for equilibrium of crystallization and amorphization varied exponentially with $1/T$, where T denoted the substrate temperature during irradiation, exhibiting the activation energy of ~ 1.2 eV, which was the characteristic of divacancy dissociation.

Upon the epitaxial growth of chemical-vapor-deposited (CVD) amorphous Si layers, La Ferla *et al.*[10] reported that they succeeded in crystallizing amorphous layers with 600-keV $^{84}Kr^{2+}$ ion irradiation at the 450 °C substrate temperature. After deposition, the samples were subsequently implanted with $1.0\times10^{15}/cm^2$, 80-keV $^{75}As^+$ ions for the purpose of mixing the interface, in order that the CVD amorphous Si layers might be crystallized easily. The author reported previously[13] that CVD amorphous Si layers could be crystallized with 2.5-MeV $^{75}As^+$ ion irradiation at the ~ 300 °C substrate temperature without mixing the interface by low-energy ion implantation. Mixing by low-energy ion implantation was not necessary, because amorphous Si layers were deposited by the clean CVD method.[14] By this method, natural oxides and contaminations on the surface of the crystalline Si substrates were clearly removed. The growth rates of CVD amorphous Si layers were $\sim 60\%$ of the low-energy ion-implantation-formed amorphous Si layers.

For the present, as reviewed in the above paragraph, an exact mechanism for the low-temperature crystallization or the layer-by-layer amorphization of amorphous Si layers has not yet been clearly determined. Now, the author will elucidate the low-temperature crystallization and the low-temperature amorphization mechanism.

Firstly, experimental results are reviewed, principally from previously published articles[11,12] along with the newly obtained results of incident energy dependence of $^{75}As^+$ ions on the recrystallized thicknesses of an amorphous Si layer. Secondly, the low-temperature crystallization mechanism and the layer-by-layer amorphization mechanism are examined in detail. The vacancy migration model, assisted by the electron-hole pair production for the electronic scattering of incident high-energy ions, explains comprehensively both the crystallization and amorphization, and is newly proposed. Reasons for differences between the author's results and other published results are also discussed. Lastly, applications of this ion-beam-induced low-temperature crystallization method are referred to; emphasis is especially put on the application to the silicon-on-insulator (SOI) structure, due to its very low crystallization temperature and low thermal stress.

II. RESULTS

In this section the experimental results[11,12] of the crystallization and layer-by-layer amorphization of amorphous Si layers on the crystalline Si substrates by high-energy heavy-ion beam irradiation are reviewed, along with the newly obtained results of incident energy dependence of the $^{75}As^+$ ions on the recrystallized thickness. The 2-in. Si (100) and (111) wafers were implanted by the 50-keV $^{75}As^+$ ions with a $5.0\times10^{15}/cm^2$ dose, and 100-keV $^{75}As^+$ ions with a $1.0\times10^{15}/cm^2$ dose to form $\sim$650- and $\sim$1150-Å-thick amorphous Si layers on the crystalline Si substrates.

The crystallinities of the low-energy ion-implanted samples and crystallized samples by high-energy ion-beam irradiation were measured by the RBS (Rutherford backscattering) channeling method. The well-collimated ($<0.03°$) 1.5-MeV probe He beam was injected to the ⟨100⟩, ⟨110⟩, and ⟨111⟩ axial channeling directions and backscattered He^+ ions were detected with a silicon surface barrier (SSB) detector of $\sim$14-keV resolution, settled at a 100°, 110°, or 170° angle to the incident probe-beam direction. The total system resolution, including the beam energy straggling from the 2.5-MeV Van de Graaff accelerator, and the preamp, main amp, and multichannel analyzer (MCA), was $\sim$20 keV, which was determined by the slope of the Si surface edge spectrum in the MCA. The horizontal axis in the MCA (channel unit) denotes backscattered He beam energy E and the vertical axis represents the number of backscattered He atoms that have energy between E and $E+\Delta E$, where ΔE is the energy width per 1 channel in the MCA. In the experimental results section, 1 channel $=\sim 4$ keV was applied to all channeling spectra.

The precise distributions of dopant ^{75}As atoms that were implanted to form $\sim$650-Å-thick amorphous Si layers by the 50-keV energy with a $5.0\times10^{15}/cm^2$ dose were also measured by the RBS method, primarily by tilting the samples at a narrow angle, for example, 5°, to the probe-beam direction. By this glancing angle backscattering method, the depth resolution was improved to 35 Å (see Sec. II B). If the normal backscattering methods (the probe He beam was injected nearly perpendicular to the sample) were adopted, the obtained depth resolution was $\sim$300 Å.

A. Crystallization of amorphous Si layer and lattice locations of dopant As atoms after crystallization

The spectra on the left in Fig. 1 show the ⟨100⟩-channeling and random spectra of a preformed $\sim$650-Å-thick amorphous Si layer and of a crystallized amorphous Si layer by 2.5-MeV $^{75}As^+$ ion irradiation with a $7.0\times10^{15}/cm^2$ dose at the ~ 290 °C substrate temperature, along with the ⟨100⟩-channeling spectrum for a bulk crystalline Si sample. The spectra on the right show the ⟨100⟩- and ⟨110⟩-channeling spectra and a random spectrum of the 50-keV-implanted ^{75}As atoms. The $\sim$650-Å-thick amorphous Si layers on the (100) Si substrates were first formed by 50-keV $^{75}As^+$ ion implantation with a $5.0\times10^{15}/cm^2$ dose.

As clearly seen in the spectra of the Si substrate, the $\sim$650-Å amorphous layer was almost completely crystallized, as far as the channeling spectrum was concerned,

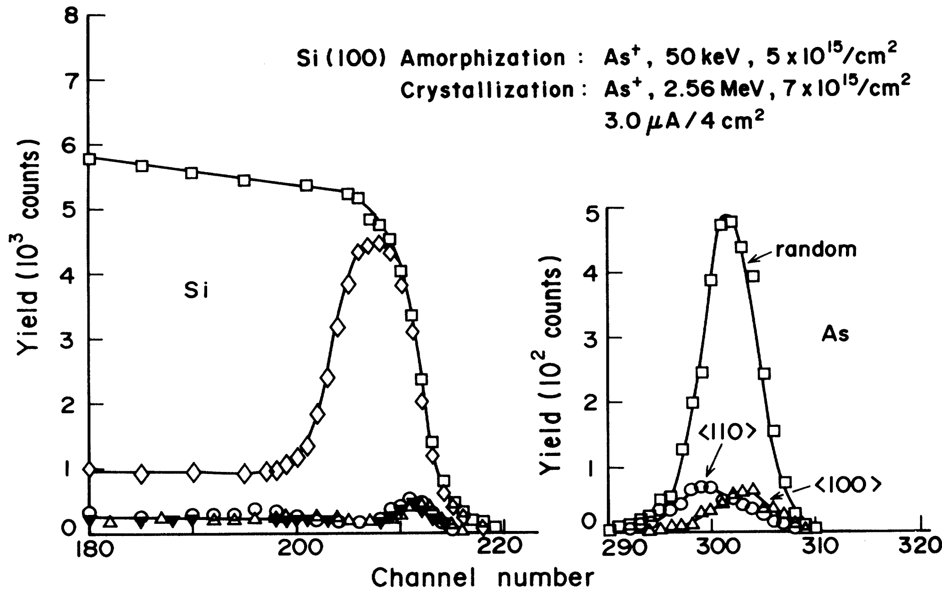

FIG. 1. ⟨100⟩- and ⟨110⟩-channeling spectra of (100) Si after crystallization by 2.56-MeV, $^{75}As^+$ ion irradiation for a $7.0\times10^{15}/cm^2$ dose with a 3.0 μA/4 cm^2 dose rate. Here, 50-keV ^{75}As spectra preimplanted to form a ~650-Å amorphous layer were also shown. □, random spectrum for the as-amorphized sample by 50-keV $^{75}As^+$ ion implantation with a $5.0\times10^{15}/cm^2$ dose; ◇, ⟨100⟩-channeling spectrum for the as-amorphized sample; △, ⟨100⟩-channeling spectrum for the crystallized sample by 2.5-MeV $^{75}As^+$ ion irradiation for a $7.0\times10^{15}/cm^2$ dose with a 3.0 μA/4 cm^2 dose rate; ○, ⟨110⟩-channeling spectrum for the crystallized sample by 2.5-MeV $^{75}As^+$ ion irradiation for a $7.0\times10^{15}/cm^2$ dose with a 3.0 μA/4 cm^2 dose rate; and ▼, ⟨100⟩-channeling spectrum for the bulk crystalline Si sample. Up to ~90% of the 50-keV-implanted dopant As atoms were located in substitutional sites and not in tetrahedral-interstitial sites.

as the channeling yields coincided with the unimplanted bulk crystalline Si sample. In the spectra on the right from 50-keV-implanted ^{75}As atoms, the areas of ⟨100⟩ and ⟨110⟩ channeling yields almost coincided, and were reduced to the ~10% of the random yields, which meant that ~90% of the 50-keV-implanted dopant ^{75}As atoms were located in substitutional sites and not in tetrahedral-interstitial sites. Therefore, ~90% of the dopant ^{75}As atoms were electrically activated. The crystallization temperature during 2.5-MeV $^{75}As^+$ ion irradiation had been kept at ~290 °C, even just under the irradiation beam spot on the Si surface, which is discussed in detail in Sec. III.

B. Precise distributions of dopant ^{75}As atoms before and after crystallization

Figure 2 shows the precise distributions of the 50-keV-implanted ^{75}As atoms before and after crystallization. The samples were tilted 5° to the probe-beam direction and detected at a 170° angle, as shown in the figure, to improve the depth resolution. The maximum depth resolution that was obtained was ~35 Å, which was one order of magnitude better than the normal RBS method.

As clearly seen in Fig. 2, both distributions almost coincided except for the extreme surface and tail region. It was impossible for dopant ^{75}As atoms to thermally diffuse deeply in the bulk or the surface of the Si substrate, because the temperature during 2.5-MeV $^{75}As^+$ ion irradiation had been kept at ~290 °C, far below the normal SPEG or LPEG temperature, even just under the irradiation beam spot. However, ^{75}As atoms moved

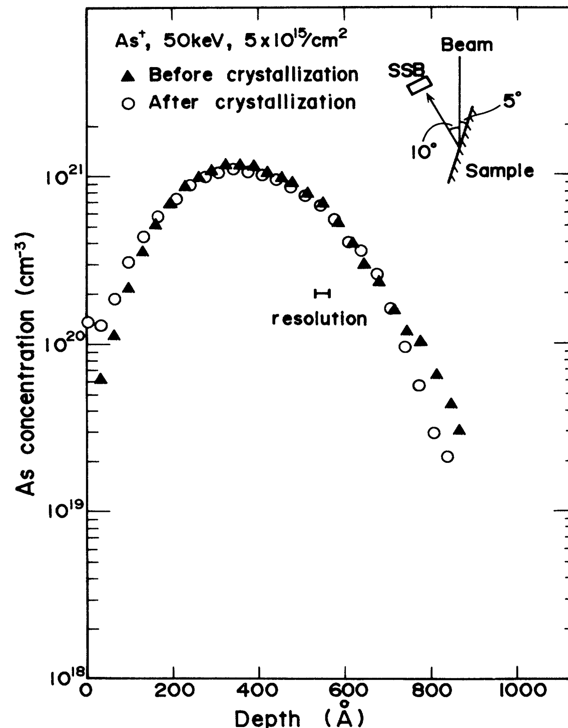

FIG. 2. Precise distributions of 50-keV ^{75}As atoms preimplanted to form a ~650-Å amorphous layer, before and after crystallization by 2.56-MeV $^{75}As^+$ ion irradiation for a $7.0\times10^{15}/cm^2$ dose with a 3.0 μA/4 cm^2 dose rate. To improve the depth resolution for ~35 Å, the glancing angle backscattering methods were adopted.

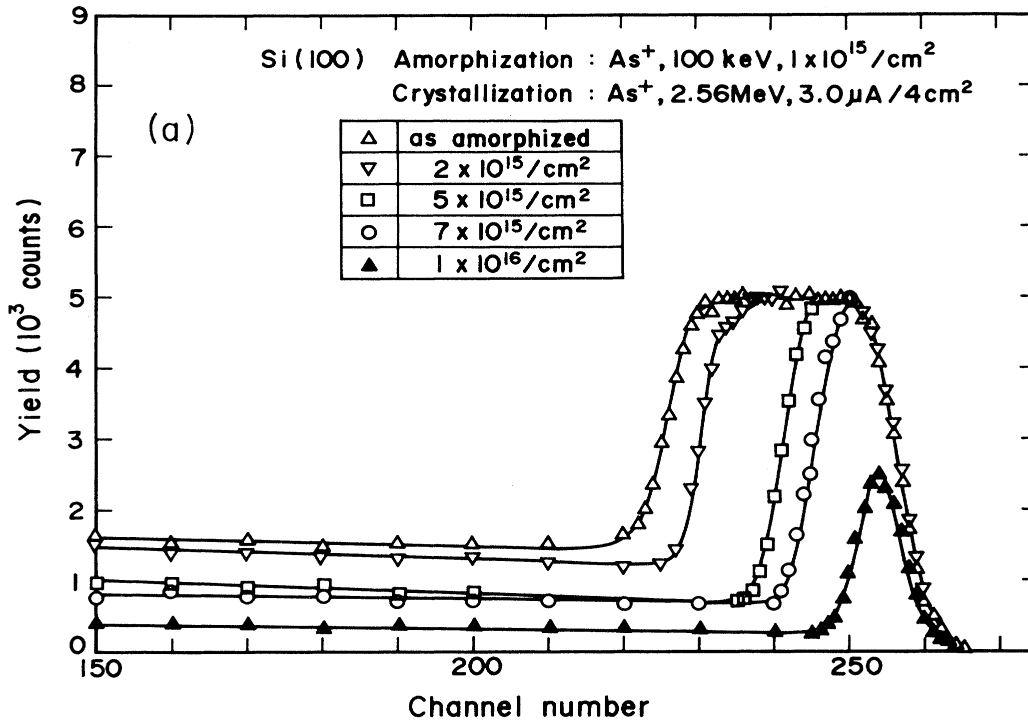

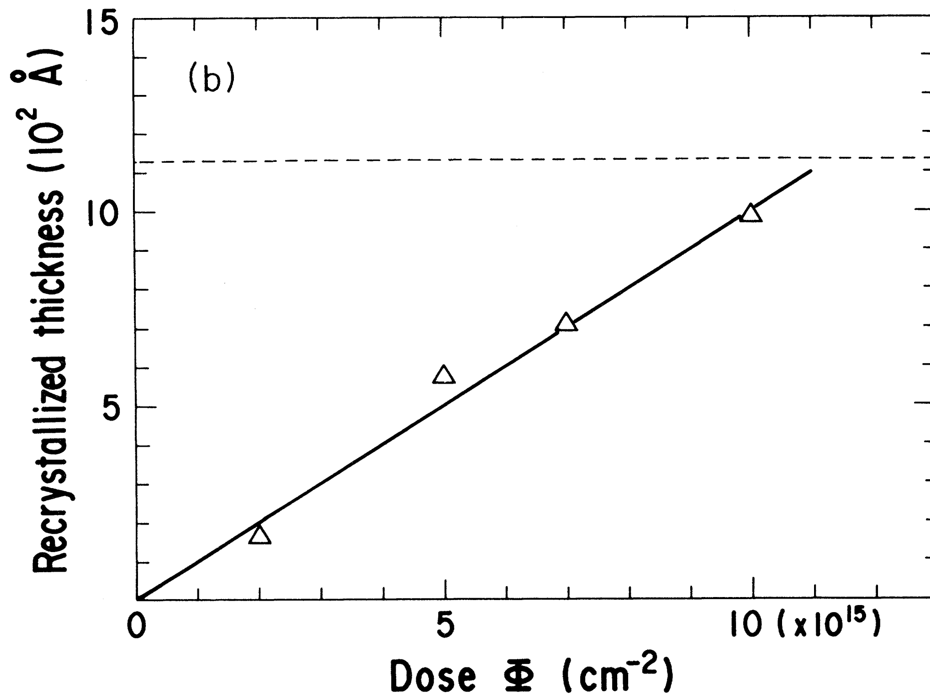

FIG. 3. (a) ⟨100⟩-channeling spectra of (100) Si after crystallization by 2.56-MeV $^{75}As^+$ ion irradiation for various doses with a 3.0 μA/4 cm^2 dose rate. The ~1150-Å amorphous layer was first formed by 100-keV $^{75}As^+$ irradiation for a 1.0×10^{15}/cm^2 dose. The amorphous layer was crystallized epitaxially. (b) The dose dependence of recrystallized thickness. The dotted line denotes first-formed amorphous-layer thickness. (c) ⟨100⟩-channeling spectra of (100) Si after crystallization by 2.56-MeV $^{75}As^+$ ion irradiation for a 5.0×10^{15}/cm^2 dose with 1.0 μA/4 cm^2 and 1.5 μA/40 cm^2 dose rates. The substrate temperatures were kept at ~185 °C for both dose rates.

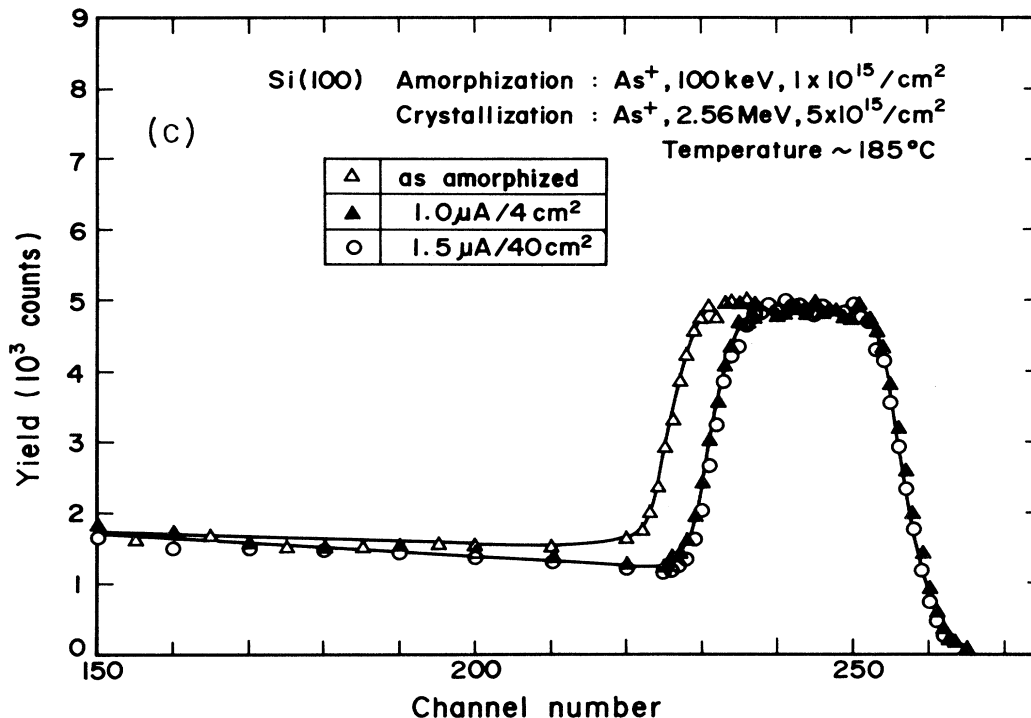

FIG. 3. (*Continued*).

slightly toward the surface, as it crystallized epitaxially. It is to be noted that the ^{75}As atoms piled up at the extreme surface after crystallization, which was first detected by the glancing angle backscattering method. The reason for this pile-up has not yet been determined, but it is clear that this phenomenon is not due to the normal thermal-diffusion process. This is a certainty because, as just stated, the ^{75}As atoms cannot diffuse at a temperature as low as ~290 °C, and no atom can diffuse toward the higher concentration region at the surface.

C. The dose and dose-rate dependence on the crystallized thickness

Figure 3(a) shows the ⟨100⟩-channeling spectra of 2.5-MeV $^{75}As^+$ ion irradiated samples with various doses at the ~290 °C substrate temperature. The ~1150-Å-thick amorphous Si layers were first formed by 100-keV $^{75}As^+$ ion implantation with a $1.0\times10^{15}/cm^2$ dose. The SSB detector was set at a 110° angle to the probe He beam to improve the depth resolution. As clearly seen in Fig. 3(a), the amorphous layer epitaxially crystallized from the crystalline-amorphous interface to the surface.

Figure 3(b) shows the dose dependence of the 2.5-MeV $^{75}As^+$ ion irradiation dose on the crystallized thickness. The dashed line denotes the thickness of the first formed amorphous layer by 100-keV $^{75}As^+$ ion irradiation. The crystallized thicknesses were proportional to the irradiation ion doses. The crystallization rate was thus obtained from the slope of this graph to be ~100 Å/($1.0\times10^{15}/cm^2$).

Figure 3(c) shows the dose-rate dependence on the crystallized thickness at the same ~185 °C substrate temperature, with 1.0 μA/4 cm² and 1.5 μA/40 cm² dose rate. The dose rate of 1.0 μA/4 cm² was conducted by irradiating 2.5-MeV annealing $^{75}As^+$ ions on a 2×2 cm² partial area of 2-in. Si wafers, through a mask put in front of the wafer holder, whereas the dose rate of 1.5 μA/40 cm² was obtained by irradiating the entire 2-in. wafer through a $\sqrt{40}\times\sqrt{40}$ cm² mask. Even if the dose rates were the same, the partial and the entire irradiation of 2-in. wafers resulted in the different wafer temperatures. This is because the partially irradiated area was cooled by the surrounding unirradiated area via conduction. On the contrary, the different dose rates resulted in the same substrate temperature. The above different dose rates were chosen so as to get the same ~185 °C substrate temperature.

As clearly seen in Fig. 3(c), the crystallized thicknesses were the same within the experimental error under these 1.0 μA/4 cm² and 1.5 μA/40 cm² dose rates at the same ~185 °C substrate temperature. Therefore, crystallization velocity should be represented in units of Å/dose and not in Å/sec, because units of Å/sec can be varied freely, as the dose rate is varied.

D. The substrate temperature dependence on the crystallized thickness

Figure 4(a) shows the ⟨100⟩-channeling spectra of 2.5-MeV $^{75}As^+$ ion irradiated samples with a $5.0\times10^{15}/cm^2$ dose at various substrate temperatures.

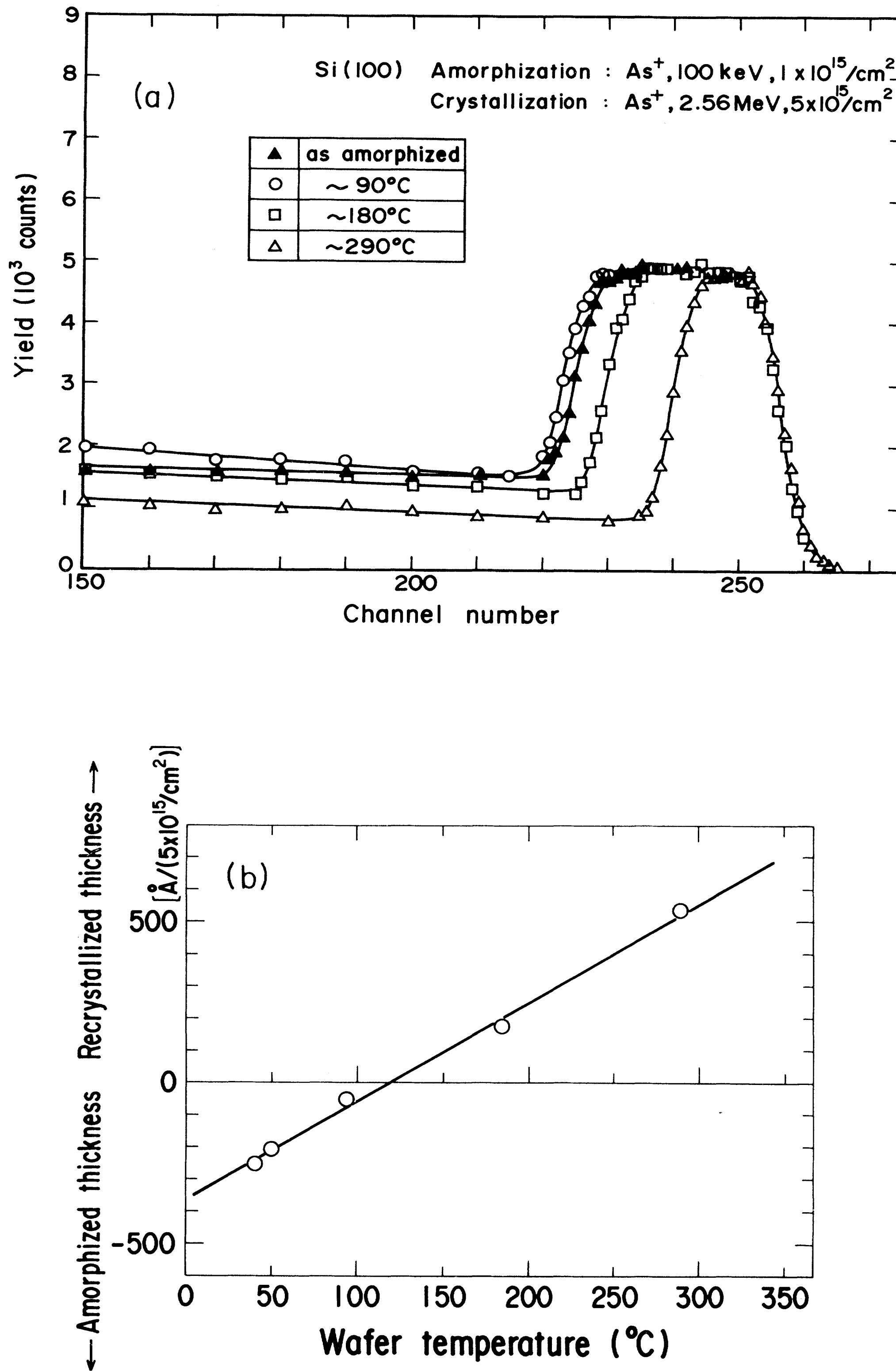

FIG. 4. (a) ⟨100⟩-channeling spectra of (100) Si after crystallization by 2.56-MeV $^{75}As^{+}$ ion irradiation for a $5.0\times10^{15}/cm^{2}$ dose with various dose rates. The substrate temperatures were varied from ~90 °C to ~290 °C by varying the dose rate. At ~90 °C, the amorphous-layer thickness was enlarged, that is, layer-by-layer amorphization occurred. (b) The substrate temperature dependence of crystallization or layer-by-layer amorphization by 2.56-MeV $^{75}As^{+}$ ion irradiation for a $5.0\times10^{15}/cm^{2}$ dose.

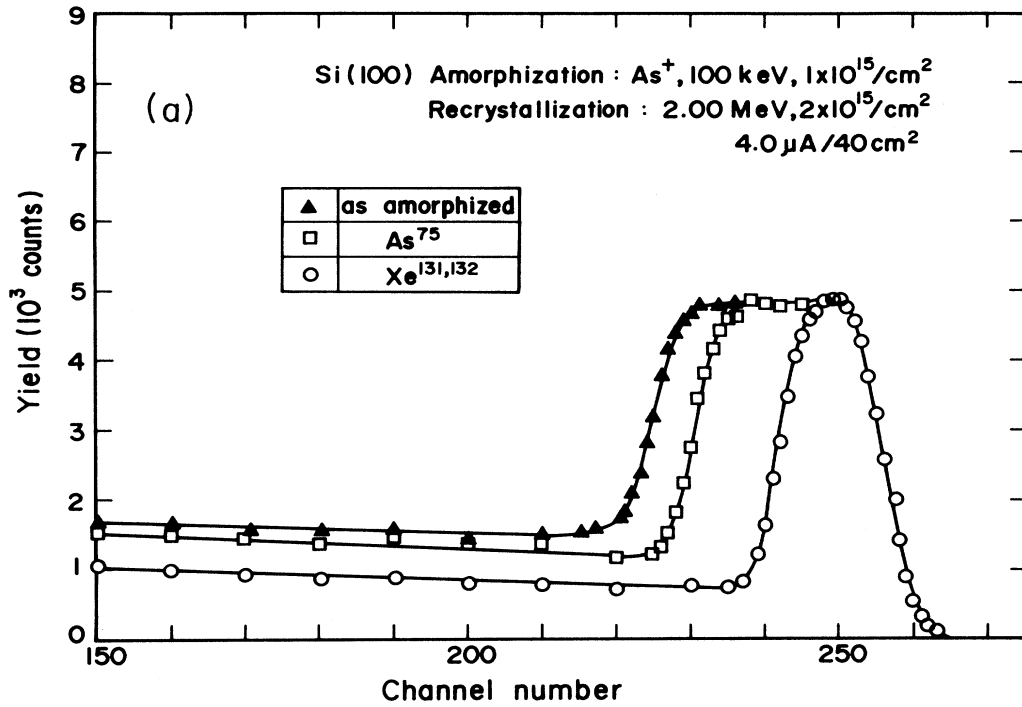

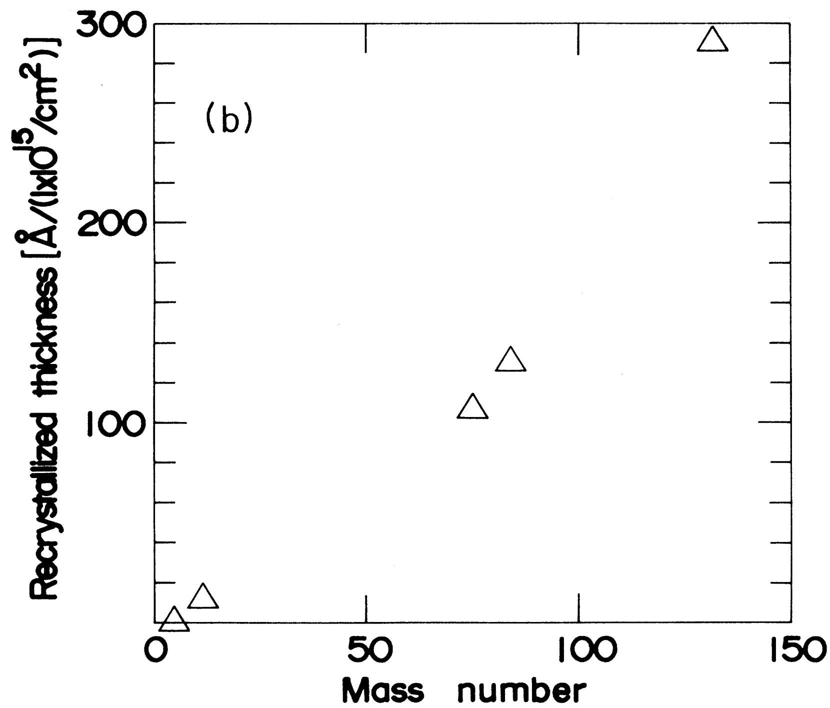

FIG. 5. (a) ⟨100⟩-channeling spectra of (100) Si after crystallization by 2.00-MeV $^{75}As^{+}$ ions and $^{131,132}Xe^{+}$ ion irradiation for a $2.0\times10^{15}/cm^2$ dose with a 4.0 $\mu A/40\ cm^2$ dose rate. (b) The mass-number dependence of the recrystallized thickness.

The $\sim$1150-Å-thick amorphous Si layers were first formed by 100-keV $^{75}As^+$ ion implantation with a $1.0\times10^{15}/cm^2$ dose. The substrate temperatures were varied by changing the beam current (dose rate) from 70 $nA/4\ cm^2$ to 3.0 $\mu A/4\ cm^2$, because the crystallized thickness was independent of the dose rate, as stated in Sec. II C.

As clearly seen from this figure, the crystallized thickness increased as the substrate temperature increased. However, the thickness of the amorphous layer was enlarged, that is, layer-by-layer amorphization occurred, when the substrate temperature was $\sim$90 °C.

Figure 4(b) shows the substrate temperature dependence on the crystallized or the amorphized thickness. The experimental results are well represented by the straight line. The results of $\sim$40 °C and $\sim$50 °C points were obtained by multiplying $\frac{5}{2}$ and $\frac{5}{3}$ of the actual experimental data obtained. In these low-temperature cases, as the extremely low beam currents ($\sim$70 nA) resulted in a long irradiation period, the irradiation doses were selected to be $2.0\times10^{15}/cm^2$ and $3.0\times10^{15}/cm^2$, assuming that the amorphization thickness was proportional to the irradiation dose, as is the same for the crystallization case in Fig. 3(a).

It is to be noted that the nuclear-energy loss of annealing 2.5-MeV $^{75}As^+$ ions at the crystalline-amorphous interface, which is proportional to the damage production in the crystalline substrate, is smaller than that in the crystalline substrate near the projected range (R_p) of annealing 2.5-MeV $^{75}As^+$ ions [see Fig. 13(a)]. Nevertheless, amorphization occurred at the interface and did not occur near the R_p. This will be discussed in more detail in Sec. III.

E. The annealing-ion-mass dependence on the crystallized thickness

Figure 5(a) shows the ⟨100⟩-channeling spectra of 2.0-MeV $^{75}As^+$ ion and 2.0-MeV $^{131,132}Xe^+$ ion irradiated samples with a $2.0\times10^{15}/cm^2$ dose at the $\sim$300 °C substrate temperature. The $\sim$1150-Å-thick amorphous Si layers were first formed by 100-keV $^{75}As^+$ ion implantation with a $1.0\times10^{15}/cm^2$ dose. The $^{131}Xe^+$ and $^{132}Xe^+$ ions were irradiated at the same time, because the present mass-analyzing magnet could not distinguish between these annealing ion masses. As clearly seen from this figure, the crystallized thickness increased as the annealing ion mass increased.

Figure 5(b) shows the annealing-ion-mass dependence on the crystallized thickness with 2.5 MeV energy at the $\sim$290 °C substrate temperature. These points represent $^4He^+$, $^{11}B^+$, $^{75}As^+$, $^{84}Kr^+$, and $^{131,132}Xe^+$ ions, respectively. Because $^{131,132}Xe^+$ ions could not be bent at 2.5 MeV energy due to the present mass-analyzing-magnet capacity, the crystallized thickness of $^{131,132}Xe^+$ ions at 2.5 MeV energy was deduced from Fig. 5(a), the 2.0-MeV annealing-ion-mass case, assuming that the crystallized thickness ratio of $^{75}As^+$ ions and $^{131,132}Xe^+$ ions in the 2.5-MeV irradiation was the same as in the 2.0-MeV irradiation in Fig. 5(a).

The light $^4He^+$ ions do not contribute to the crystallization, whereas heavy ions, such as $^{84}Kr^+$ and $^{131,132}Xe^+$ ions, crystallize amorphous Si layers a great deal. These results strongly suggest that crystallization occurred due to defects such as vacancies and interstitials produced by the nuclear scattering of annealing ions in the crystalline Si substrate under the amorphous Si layer.

F. The energy dependence on the crystallized thickness

Figure 6(a) shows the ⟨100⟩-channeling spectra of $^{75}As^+$ ion irradiated samples of various energies with a $3.0\times10^{15}/cm^2$ dose at the $\sim$170 °C substrate temperature. The SSB detector was settled at a 100° angle to get higher resolution. The 4-in. silicon wafers were first implanted by 100-keV $^{75}As^+$ ions with a $1.0\times10^{15}/cm^2$ dose to form $\sim$1150-Å-thick amorphous layers. The substrate temperature had been kept constant at $\sim$170 °C by varying the beam currents as the irradiation energies changed, so that the input power densities on the silicon wafers might become the same values. Because the target chamber structure had been changed when the energy-dependence experiments were undertaken (cf. Sec. IV B), the wafer temperature could not be raised above $\sim$170 °C, though the incident beam power was greater than in other experimental cases.

As shown in this figure, the crystallized thickness increased as the irradiation energy increased. The 1.54- and 2.00-MeV irradiation doses resulted in almost the same crystallization thicknesses. However, in the 2.56-MeV irradiation case, the crystalline-amorphous interface more clearly proceeded to the surface than in the other energy cases.

Figure 6(b) shows the energy dependence on the crystallized thickness (arbitrary units). Evidently, the crystallized thickness was larger with 2.56-MeV irradiation, but almost the same with 2.00- and 1.54-MeV irradiation. Although thoroughly precise energy-dependence experiments with the higher doses and at the higher substrate temperatures were desirable, it could be concluded that in the $^{75}As^+$ ion irradiation case, the crystallized thickness increased as the incident energy increased.

G. The substrate orientation dependence on the crystallized thickness

Figure 7 shows ⟨100⟩- and ⟨111⟩-channeling spectra of (100) and (111) Si wafers irradiated by 2.5-MeV $^{75}As^+$ ions with a $5.0\times10^{15}/cm^2$ dose at the $\sim$290 °C substrate temperature. The $\sim$1150-Å-thick amorphous Si layers were first formed by 100-keV $^{75}As^+$ ion implantation with a $1.0\times10^{15}/cm^2$ dose.

As clearly seen from this figure, the crystallized thickness of the (100) Si wafer was approximately two times larger than that of the (111) Si wafer. In the normal SPEG of furnace annealing, the growth rate is approximately 25 times larger for (100) than for (111) Si.[19] Therefore, a completely different crystallized mechanism must be considered in this high-energy heavy-ion beam irradiation at the substrate temperatures below $\sim$300 °C.

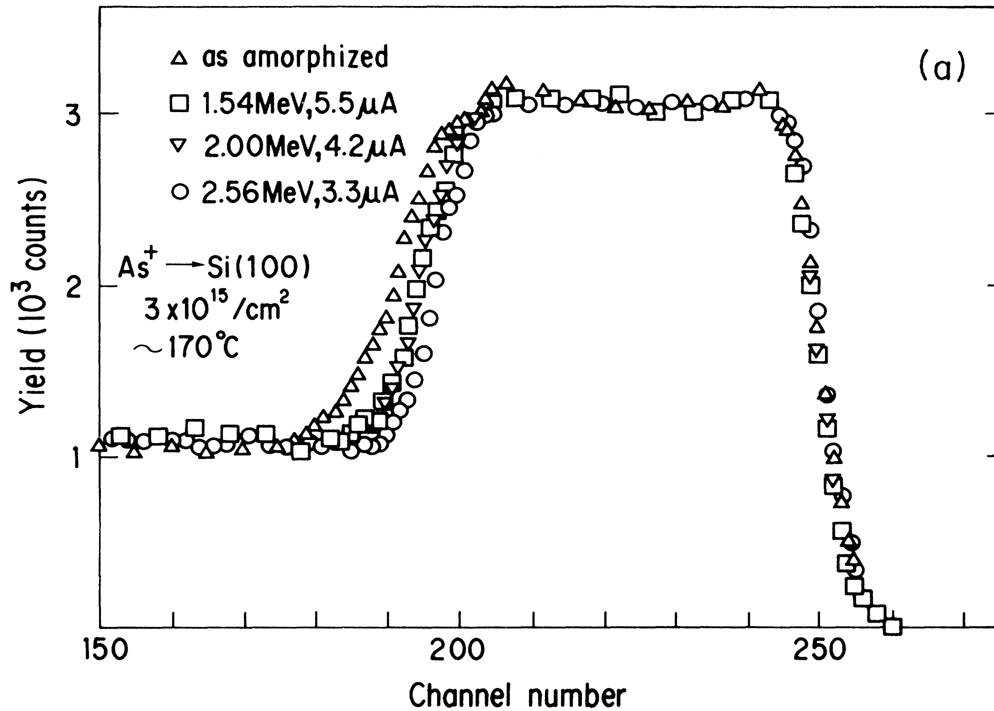

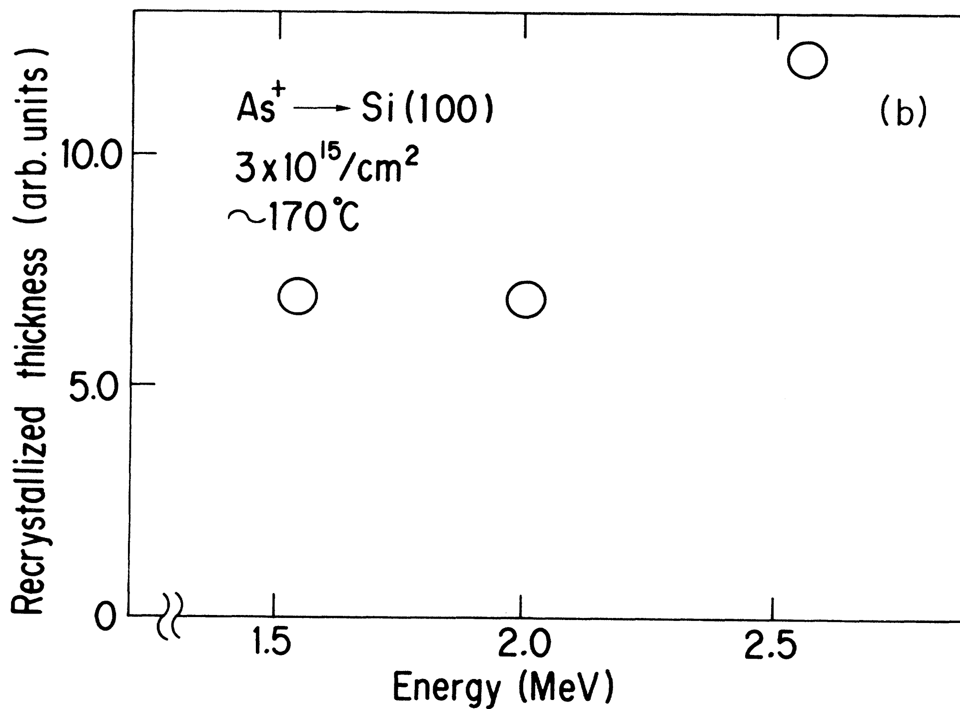

FIG. 6. (a) ⟨100⟩channeling spectra of (100) Si after crystallization by $^{75}As^+$ ion irradiation for a $3.0\times10^{15}/cm^2$ dose with various irradiation energies. The beam currents (dose rates) were varied so that the substrate temperatures might be the same value of $\sim170\,^{\circ}C$ for different irradiation energies. The scanning area on the wafer was 62 cm^2, so that the influence of the transient wafer temperatures or the dose rates on the recrystallized thickness might be avoided. (b) The irradiation energy dependence of $^{75}As^+$ ions on the recrystallized thickness.

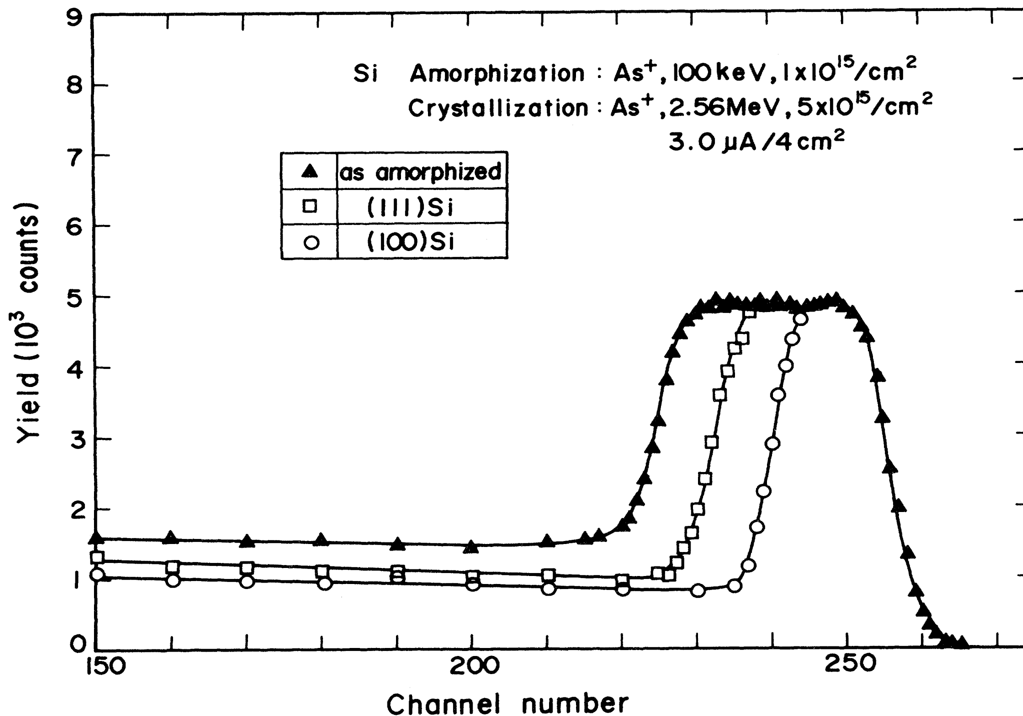

FIG. 7. ⟨100⟩- and ⟨111⟩-channeling spectra of (100) and (111) Si after crystallization by 2.56-MeV $^{75}As^+$ ion irradiation for a $5.0\times10^{15}/cm^2$ dose with a 3.0 μA/4 cm^2 dose rate.

H. The dose dependence on the crystallized thickness of CVD amorphous Si layer

In the above sections the amorphous Si layers were all low-energy (50–100-keV) ion-implantation-formed amorphous layers. In this section the amorphous layers were formed by the CVD method.

Figure 8 shows the channeling spectra of 2.5-MeV $^{75}As^+$ ion irradiated CVD amorphous Si layers, with various doses, at the ~300 °C substrate temperature. The ~1500-Å-thick CVD amorphous Si layers were deposited by the clean-CVD method.[14] Using this method, natural oxides and contaminants at the crystalline-amorphous interface were clearly removed.

As clearly seen from this figure, the CVD amorphous Si layers were also epitaxially crystallized to the bulk crystalline Si at the very low ~300 °C substrate temperature, as far as the channeling spectra were concerned. The crystallized thickness was proportional to $^{75}As^+$ ion doses. However, the crystallization rate was ~60% that of the low-energy ion-implantation-formed amorphous Si layers. The crystallization rate would be improved to a rate near that of the ion-implantation-formed amorphous Si layers, if thorough cleaning procedures were adopted at deposition.

In concluding this section, the experimental results were summarized as follows.

(1) The crystallization of amorphous Si layers occurred at the very low substrate temperature of ~300 °C by high-energy (1.0–2.5-MeV) heavy-ion ($^{75}As^+$, $^{84}Kr^+$, $^{131,132}Xe^+$) beam irradiation, far below the ordinary SPEG or LPEG temperatures of ~600 °C and ~1400 °C, respectively. Up to ~90% of the dopant ^{75}As atoms in the amorphous layer were located in substitutional sites and not in tetrahedral-interstitial sites after crystallization, and were electrically activated. The distribution of dopant ^{75}As atoms did not change before or after crystallization.

(2) The crystallized thickness was proportional to the irradiation ion dose and independent of the dose rate.

(3) The crystallized thickness increased as the irradiation ion energy and mass increased.

(4) When the irradiated annealing ions were 2.5-MeV $^{75}As^+$, the crystallization thickness increased as the substrate temperature increased in the range of 120–300 °C, and the layer-by-layer amorphization occurred when the substrate temperatures were below ~120 °C.

(5) The crystallization rate of (100) Si was approximately two times larger than that for the (111) Si.

(6) The CVD amorphous Si layers could also be crystallized at the ~300 °C substrate temperature; however, the crystallization rate was ~60% that of the ion-implantation-formed amorphous Si layers.

III. DISCUSSIONS AND SPECULATIONS

In this section the author minutely clarifies and speculates about the mechanism of low-temperature

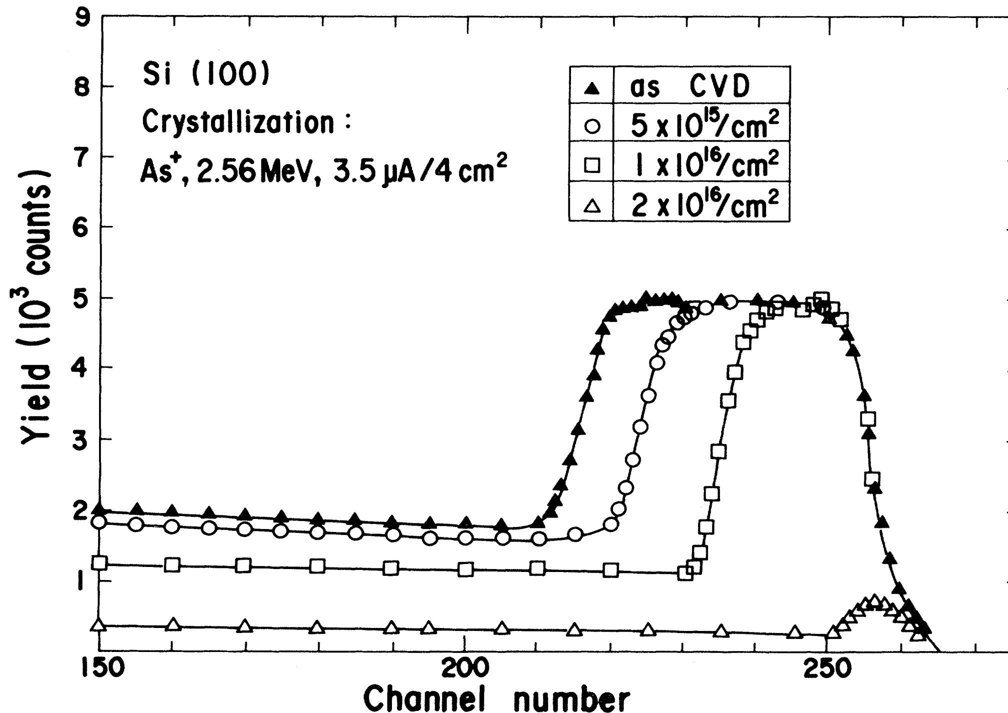

FIG. 8. ⟨100⟩-channeling spectra of (100) Si after crystallization of CVD amorphous Si by 2.56-MeV $^{75}As^{+}$ ion irradiation for various doses with a 3.5 μA/4 cm^2 dose rate.

(120–300 °C, in the 2.5-MeV $^{75}As^{+}$ irradiation case) crystallization of amorphous Si layers on the crystalline Si substrates, and the mechanism of layer-by-layer amorphization at low temperature (≤120 °C, in the 2.5-MeV $^{75}As^{+}$ irradiation case).

Firstly, the Si wafer temperatures during high-energy heavy-ion beam irradiation are measured and calculated. The author emphasizes that even just under the irradiation beam spot, the temperature has been kept below the ~300 °C equilibrium temperature.

Secondly, the vacancy (produced by the elastic nuclear scattering of incident ions) migration model in the crystalline substrate under the amorphous layer, assisted by the electron-hole pair production (formed by the inelastic electronic scattering of incident ions), is proposed, which comprehensively explains both the crystallization and the layer-by-layer amorphization. Lastly, the author discusses the differences between these results and other published results.

A. The Si wafer temperatures during irradiation

1. The equilibrium wafer temperatures measured by heat labels

The equilibrium wafer temperatures during irradiation were measured by heat labels attached to the back side of wafers. Figure 9 shows the dependence of the wafer temperature on the input power density of the irradiation beam. The vertical bars signify the measured values and the curved lines represent the calculated temperatures for various effective emittances.

As clearly seen from this figure, the equilibrium wafer temperatures increase as the input power densities increase; however, they are kept below ~300 °C. The input power density can be deduced by multiplying the beam

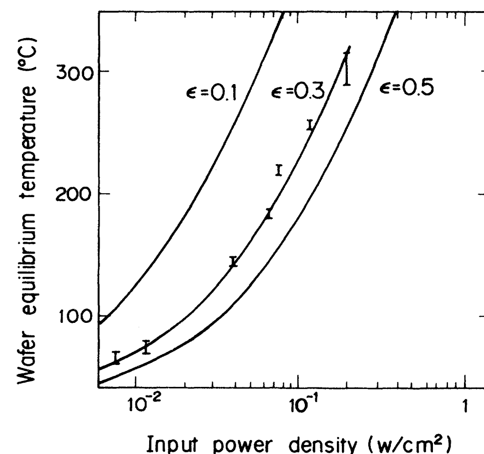

FIG. 9. The equilibrium wafer-temperature dependence on the input power density measured by heat labels attached to the back side of wafers, and calculated values for various effective emittances.

current by the irradiation energy and dividing by the scanning area. The maximum input power density for a normal 40-cm^2 scanning area is

$$(2.5\ \mathrm{MeV})\times(3.0\ \mu\mathrm{A})/40\ \mathrm{cm}^2=0.185\ \mathrm{W/cm}^2 .$$

Using a 4-cm^2 area mask to shorten the irradiation period, the maximum is deduced to be 1.85 W/cm^2. However, the experimentally measured temperature for this partial area irradiation was also ~300 °C, due to the cooling effect via conduction from the unirradiated area of the wafer. The author also ascertained that the wafer temperatures showed the same values between the same incident power with different current-energy combinations. The calculation procedures for obtaining the wafer equilibrium temperature are as follows.

Because the back side of Si wafers were not tightly attached to the wafer holder, the input power of the high-energy beam is dissipated almost by radiation in the vacuum. Although the actual wafer-holder structures including the target chamber are uneven and complicated, the author uses the simplified equation that holds among the infinite area planes settled in parallel,[15]

$$P_b=\epsilon\sigma(T^4-T_s^4) , \quad (1)$$

where P_b is the input power density by irradiation beam, ϵ is the effective emittance of the Si wafer, σ is the Stephan-Boltzmann constant of 5.67×10^{-12} W/cm^2, T is the substrate Si wafer temperature, and T_s is the surrounding target chamber temperature. The effective emittance ϵ is the fitting parameter introduced to simplify Eq. (1). Assuming that the emittances of the Si wafer surface, the back side of the wafer, the wafer holder, and the internal surface of the target chamber are ϵ_{w1}, ϵ_{w2}, ϵ_h, and ϵ_s, respectively; the total effective emittance ϵ can be represented as the following equation:

$$\epsilon=\epsilon_{w1}\epsilon_s/[\epsilon_s+\epsilon_{w1}(1-\epsilon_s)]+\epsilon_{w2}\epsilon_h/[\epsilon_h+\epsilon_{w2}(1-\epsilon_h)] . \quad (2)$$

For example, if we assume that $\epsilon_{w1}=\epsilon_{w2}=0.28$ and $\epsilon_h=\epsilon_s=0.75$, then we get $\epsilon=0.52$ for the effective emittance. Actually, this effective emittance ϵ is determined in order that the T, deduced by the above equation (1), might fit the experimentally measured temperatures (vertical bars in Fig. 9). Thus, ϵ, under these experimental conditions, is determined to be 0.3, as is clearly seen in the middle line in Fig. 9.

2. The transient wafer temperatures calculated using $\epsilon=0.3$

Because the wafer holders are not equipped with heaters to warm up the Si wafers, the Si substrates can be warmed by an irradiation high-energy beam only. Therefore, the wafer has been kept at room temperature in the initial stage of irradiation. This suggests the transient heat hysteresis. So, in order to clarify the influence of the heat hysteresis, the author calculated the transient heat characteristics, using the above obtained effective emittance of $\epsilon=0.3$.

The increase rate of the Si wafer temperature during irradiation can be determined by the difference between the input power density and the heat dissipation via radiation, divided by the heat capacity of the wafer. Therefore, the following equation holds:

$$dT/dt=[P_b-\epsilon\sigma(T^4-T_s^4)]/(\rho LC) , \quad (3)$$

where ρ is the Si wafer density, L is the Si wafer thickness, and C is the heat capacity.

Equation (3) can be variably separated as follows:

$$dt=dT/[a(T^4-b)] , \quad (4)$$

where $a=-\epsilon\sigma/(\rho LC)$ and $b=P_b/(\epsilon\sigma)+T_s^4$. The differential equation (4) can be precisely solved as follows:

$$t=b^{-3/4}[0.5\ln|(T-b^{1/4})/(T+b^{1/4})| - b^{-1/4}\tan^{-1}(t/b^{1/4})]_{T_s}^{T(t)}/(2a) . \quad (5)$$

Here, the initial condition is $T=300$ K of room temperature as $t=0$.

The calculated results of Eq. (5) are shown in Fig. 10. In this calculation, the L is assumed to be 0.02 cm (the thickness of a 2-in. wafer) and the effective emittance ϵ is to be 0.3 as obtained in Sec. III A 1; the surrounding temperature T_s of the target chamber is to be 300 K. In Fig. 10 the represented parameters are the input power densities or the beam currents when the irradiation energy is constant at 2.5 MeV. As clearly seen from this figure, the Si wafer temperatures reach their equilibrium values in several tens of seconds for any input power density. In Fig. 10 the irradiation doses are also denoted by dotted lines for the 40-cm^2 area scanning case. As mentioned in Sec. II, the irradiation doses in the present experiments were all in the range of 2.0×10^{15}/cm^2–2.0×10^{16}/cm^2, which means that the irradiation periods were all in the range of 7–70 min even if a 4-cm^2 mask was used. Therefore, only in the initial stage of irradiation were the Si wafers put under the low-temperature transient conditions. Almost for the entire time during irradiation, the

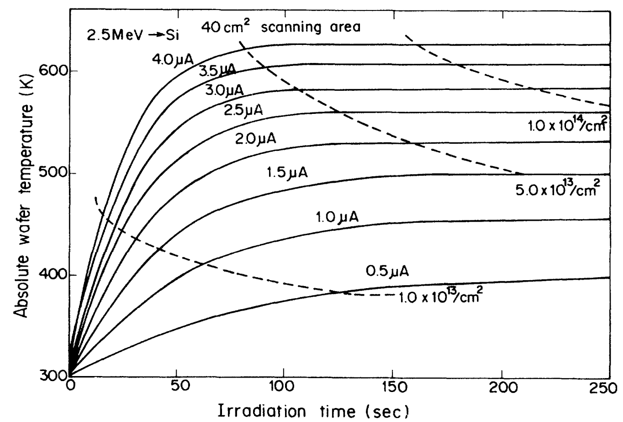

FIG. 10. The transient wafer temperature for various input power densities calculated using an effective emittance of 0.3.

wafers had been kept at the equilibrium temperature. Thus, the experimental results discussed in Sec. II are not influenced by the transient temperature characteristics. However, as will be discussed in detail in Sec. IV B, it is only in the case of the irradiation energy dependence experiment that the transient wafer temperature characteristics cannot be neglected below the ~1.5-MeV irradiation energy, using a 4-cm^2 area mask.

3. *The wafer temperature just under the irradiation beam spot*

The temperatures discussed in Secs. III A 1 and III A 2 were the macroscopic total wafer temperatures of equilibrium and transient states of irradiation. In this subsection the local and instantaneous wafer temperature just under the irradiation beam spot on the Si surface is considered.

Figure 11 is a schematic view of the scanned irradiation beam. The typical irradiation conditions are as follows: The diameter of the beam spot is ~10 mm, the spot beam current is ~5 μA, and the scanning speed is ~10^4 cm/sec. The scanning beam current on the wafer is ~3 μA at the maximum, which is below the spot beam current, because the beam spot is overscanned on the wafer so that the total area of the wafer will be irradiated uniformly.

The experimentally obtained projected range (R_p) of 2.5-MeV $^{75}As^+$ ions was ~1.6 μm. If the total input power was consumed adiabatically in a cylindrical volume of 10 mm diameter and 1.6 μm height of the Si wafer within 10^{-4} sec (the period that was deduced from the 10^4-cm/sec scanning speed and the 10-mm beam spot diameter), the local and instantaneous temperature rise just under the irradiation beam spot, compared with the surrounding equilibrium Si wafer temperature, was deduced to be only ~20 °C, assuming that the Si heat capacity was 0.168 cal/deg g. This value was overestimated, because the author assumed that all the input power was consumed adiabatically. In reality, the heat is dissipated via conduction in the Si wafer and via radiation in the vacuum; the temperature rise is anticipated to be much lower than ~20 °C. The precise calculation[16] including conduction predicts that the temperature rise is below ~1 °C. In conclusion, the wafer temperatures had been kept under the equilibrium ~300 °C substrate temperature without the local and instantaneous temperature rise just under the irradiation beam spot.

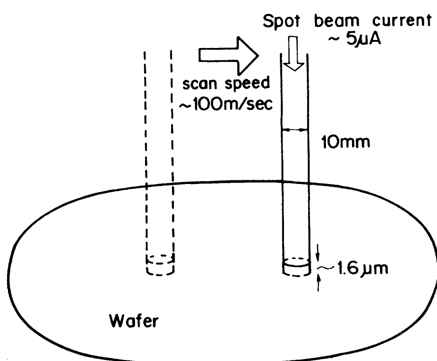

FIG. 11. The schematic view for representing the scanning beam spot.

4. *Thermal spikes*

Thermal spikes[17] are localized and instantaneous heating around each incident ion track. The diameter of each spike is supposed to be ~40 Å and the time constant or the lifetime of tracks, ~5.5×10^{-10} sec. For comparison, the 2.5-MeV incident high-energy ion stops at the R_p of ~1.6 μm depth within ~1.0×10^{-13} sec.

If these spikes contributed to the crystallization of amorphous Si layers on the crystalline Si substrates, the crystallization rate would not depend so largely on the equilibrium wafer temperature, as mentioned in Sec. II D. Much more, the layer-by-layer amorphization would not by any means occur at the low wafer temperature. That is, if such microscopic thermal spikes around each ion track contributed to the "low-temperature" crystallization, the crystallization rates would not depend on the macroscopic equilibrium wafer temperature.

In conclusion, it was ascertained that the amorphous Si layers on the crystalline Si substrates were undoubtedly crystallized by ion beam irradiation below the SPEG temperature of amorphous Si and without a localized and instantaneous temperature rise both just under the irradiation beam spot on the Si surface and around each incident ion track.

B. The low-temperature (120–300 °C) crystallization mechanism

It is clarified in this section that the low-temperature crystallization occurs by supplying vacancies, produced by the nuclear scattering of incident ions in the crystalline substrate, to the amorphous layer via thermal diffusion, which become the "vacant spaces" in the amorphous layer near the crystalline-amorphous interface. Then, "vacant spaces" induce redistribution of amorphous Si atoms near the crystalline-amorphous interface, resulting in layer-by-layer crystallization at low temperature.

1. *Crystallization by vacancy migration*

Figure 12(a) shows the layer-by-layer crystallization model by high-energy heavy-ion beam irradiation. The crystallization procedures are mentioned in sequence, as follows.

(1) The high-energy heavy ions penetrate deeply (1–2 μm) in the crystalline Si substrate through the surface amorphous Si layer (~0.1 μm thickness) and produce a lot of vacancies and interstitials around the ion tracks in the crystalline substrate under the amorphous layer. The open and solid circles represent vacancies and interstitial Si atoms produced by incident ions. The dotted circles denote normal Si atoms positioned in the lattice sites.

The vacancy concentration is higher in the near center

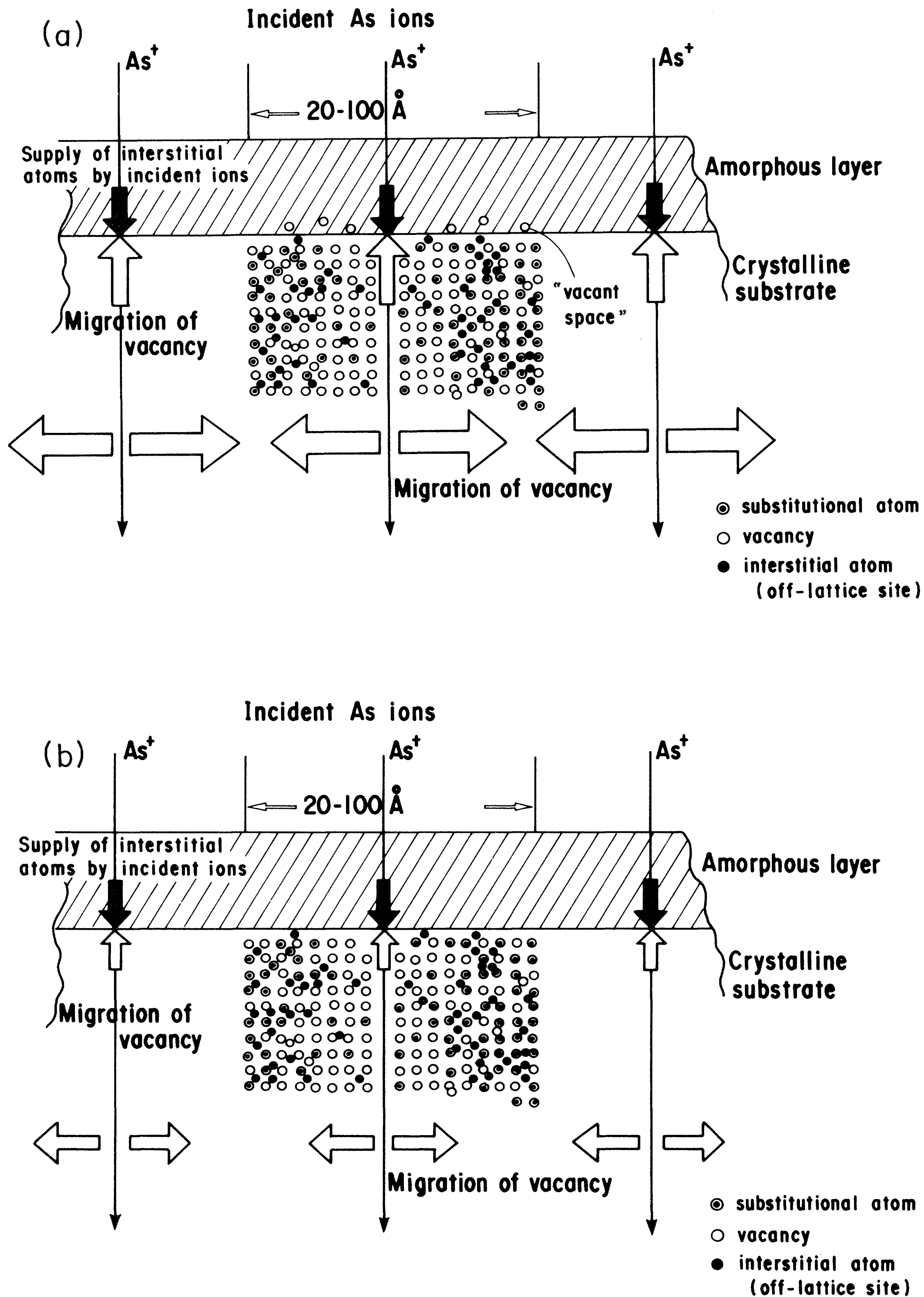

FIG. 12. (a) The low-temperature crystallization mechanism model of the amorphous Si layer on the crystalline Si substrate by beam irradiation, showing that the vacancy supply surpasses the knocked-on interstitial Si atom supply at the crystalline-amorphous interface. (b) The low-temperature layer-by-layer amorphization mechanism model of the amorphous Si layer on the crystalline Si substrate, showing that the vacancy supply decreases as the equilibrium wafer temperature decreases, due to the temperature dependence of the thermal-diffusion coefficient for vacancies, whereas the supply of knocked-on interstitial Si atoms does not vary because it was determined only by the incident energy and ion species and not by the equilibrium wafer temperature.

of the ion tracks than in the surrounding region around the ion tracks, because incident ions knock on the Si atoms from their normal lattice sites to the interstitial sites (off-lattice sites) along the ion tracks. Therefore, cylindrical damaged regions around each ion track, 20–100 Å in diameter, are formed in which vacancies are rich in the center and interstitial atoms are rich in the surrounding regions. The cylindrical damaged regions are formed within the $\sim 1.0\times 10^{-13}$ sec duration for incident ions to be stopped.

(2) The vacancies migrate via thermal diffusion, from the center of the vacancy-rich region to the surrounding interstitial-rich region in the cylindrical damaged volumes around the ion tracks. The diffusion coefficient is determined by the equilibrium wafer temperature. The radial directions in the cylindrical volumes perpendicular to the ion track, denoted by larger open arrows, show the vacancy thermal-diffusion movement.

After the radial vacancy diffusion, the center of the cylindrical damaged region crystallizes because the vacancies are replaced by Si atoms in normal lattice positions. These migrated vacancies recombine with the interstitial Si atoms in the interstitial-rich region of the cylindrical volumes. That is, the cylindrical damaged regions in the crystalline substrate under the amorphous layer recrystallize by the vacancy diffusion and recombination processes. These migration and recombination procedures are completed within $\sim 1.0\times 10^{-9}$ sec.[18]

(3) The vacancies also migrate to the surface amorphous Si layer, so to speak, to the assembly for interstitial Si atoms. These movements are denoted by rather small open arrows parallel to the incident ion tracks. On the contrary, interstitial Si atoms knocked on by incident energetic ions are supplied to the crystalline substrate from the amorphous layer. These are represented by solid arrows. These migrated vacancies from the crystalline substrate and knocked-on interstitial Si atoms from the amorphous layer combine at the crystalline-amorphous interface.

(4) After combination at the crystalline-amorphous interface, vacancies or interstitial Si atoms are left. If open arrows (proportional to the number of vacancies supplied to the amorphous layer) are larger than solid arrows (proportional to the number of knocked-on interstitial Si atoms supplied to the crystalline substrate), vacancies are left and they are supplied to the amorphous layer. Supplied vacancies are not actual vacancies but are "vacant spaces" in the amorphous layer. The word "vacancy" is valid only in the crystalline and not in the amorphous layer. The number of vacant spaces in the amorphous layer near the interface increases as incident ions are supplied continuously. These vacant spaces make the thermal vibrations of Si atoms in the amorphous layer near the interface more free, and induce redistribution of Si atoms, resulting in the crystallization of one monolayer at the interface. During ion beam irradiation, vacancies are supplied continuously from the crystalline substrate and the next monolayer crystallizes. Thus, the layer-by-layer epitaxial crystallization occurs at a low temperature ($\leq 300\,^{\circ}$C), far below the normal SPEG temperature ($\sim 600\,^{\circ}$C).

Thus, the reason for the low-temperature crystallization is that vacancies migrate easily at low temperature ($\leq 300\,^{\circ}$C) and vacant spaces in the amorphous layer induce redistribution of thermal-vibration-free Si atoms in the amorphous layer near the crystalline-amorphous interface at low temperature ($\leq 300\,^{\circ}$C), resulting in epitaxial crystallization. Therefore, a supply of vacancies to the amorphous layer is essential for low-temperature layer-by-layer epitaxial crystallization.

2. *Vacancy migration assisted by the production of electron-hole pairs*

The activation energy of layer-by-layer epitaxial crystallization by high-energy heavy-ion beam irradiation is deduced to be ~ 0.2 eV from the slope of the substrate temperature dependence on the crystallized thickness in Fig. 4(b), though only the two points of $\sim 180\,^{\circ}$C and $\sim 290\,^{\circ}$C are available. This low ~ 0.2-eV activation energy is much smaller than the 2.3-eV (Ref. 19) normal SPEG activation energy by furnace annealing. The ~ 0.2 eV activation energy coincides with the 0.24 eV that Williams *et al.*[7] proposed, when they irradiated amorphous Si layers on the crystalline substrates by 0.6–3.0-MeV $^{20}Ne^{+}$ ions at the temperature range of 200–300 °C.

The activation energy of ~ 0.2 eV also coincides with 0.18 eV of the migration of doubly negative vacancies in the crystalline Si substrate proposed by Watkins.[20] Doubly negative vacancies are more mobile than neutral vacancies in which the activation energy for migration is 0.33 eV.[20] Therefore, the more vacancies produced by the incident ions and the more doubly negative vacancies, the more the recrystallization rate of the amorphous Si layer increases.

As the irradiation energy increases, the ratio of the deposited energy by the inelastic electronic scattering, for ionization and excitation, to the deposited energy by the elastic nuclear scattering increases. The nuclear and electronic deposited energy density (ENDED: elastic nuclear deposited energy density; IEDED: inelastic electronic deposited energy density) distributions of $^{75}As^{+}$ ions in Si for various incident ion energies are shown in Figs. 13(a) and 13(b).[21] It is clear from these figures that the ENDED at the surface decreases as the incident energy increases, because the nuclear scattering cross section is reduced. In contrast, the IEDED at the surface becomes large, as the irradiation energy increases. Therefore, the number of electron-hole pairs produced by the inelastic scattering increases as the ion energy increases, and initially formed neutral vacancies produced by the elastic nuclear collision are liable to be converted to doubly negative vacancies V^{2-} for dense electron-hole pairs around vacancies.

As mentioned in Sec. II, the recrystallization rate increased as the incident ion mass increased. This is because the ratio of the nuclear scattering becomes high, and contributes to the production of a lot of vacancies in the crystalline substrate under the amorphous layer. It was also mentioned that the recrystallization rate increased as the incident ion energy increased. This is because the number of electron-hole pairs increases and

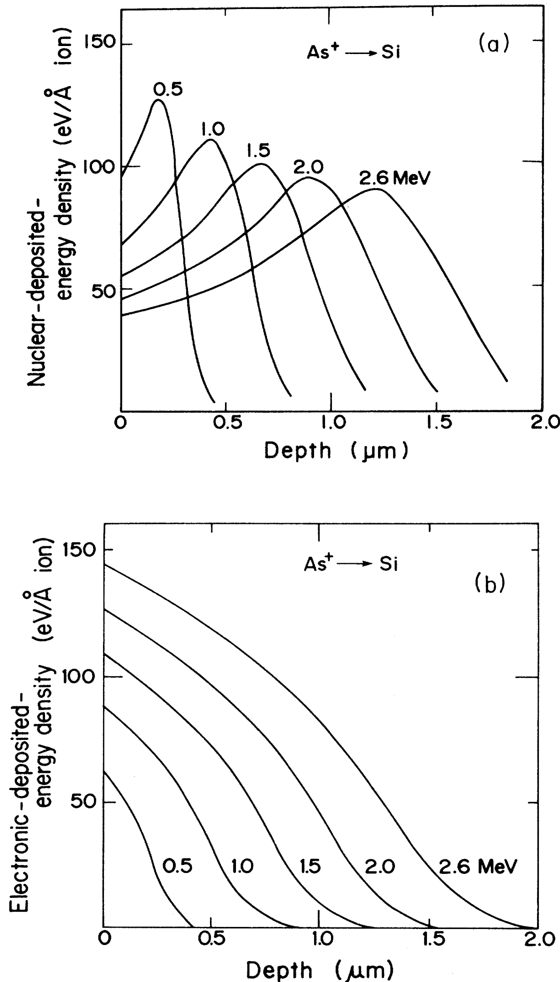

FIG. 13. (a) The calculated elastic nuclear deposited energy density distributions of $^{75}As^+$ ions for various incident energy in Si. (b) The calculated inelastic electronic deposited energy density distributions of $^{75}As^+$ ions for various incident energy in Si.

enhances to convert neutral vacancies to more mobile doubly negative vacancies.

If only the vacancy concentration contributed to the recrystallization rate, the recrystallized thickness should decrease with an increase in incident ion energy, because the ENDED (proportional to the vacancy concentration) at the crystalline-amorphous interface (at ~ 0.1 μm depth) decreases as the incident energy increases [see Fig. 13(a)]. This is shown by the dotted line (solid circles) in Fig. 14. The solid circles represent the ENDED at the crystalline-amorphous interface in an arbitrary unit, which are plotted to coincide with the experimental crystallization rate at 1.5-MeV irradiation energy. Experimentally, the recrystallized thickness increases as the incident energy increases, as shown by the open circles in Fig. 14.

Therefore, for crystallizing amorphous layers at low temperature, it is necessary that the irradiation ion mass

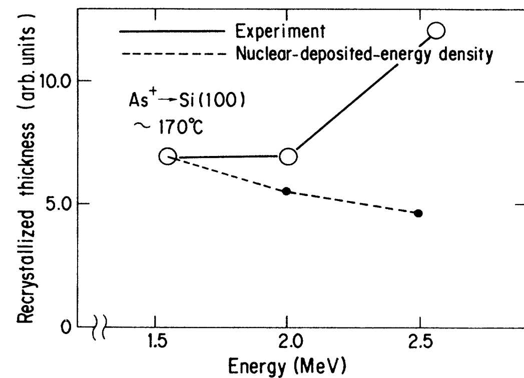

FIG. 14. The experimentally measured (solid line) and calculated (dashed line) irradiation energy dependence on the recrystallized thickness. The calculation assumed that the recrystallized thickness was proportional to the vacancy concentration at the crystalline-amorphous interface. It also assumed that the vacancy concentration at the interface was proportional to the elastic nuclear deposited energy density at the interface.

be heavy enough to produce vacancies. Furthermore, by accelerating the irradiation energy, the amorphous layers crystallize effectively. In Sec. III C, the layer-by-layer amorphization process is discussed, which does not conflict with the above-mentioned crystallization mechanism.

C. The layer-by-layer amorphization mechanism at low temperature (≤ 120 °C)

Layer-by-layer amorphization occurred at low temperature (≤ 120 °C in the 2.5-MeV $^{75}As^+$ irradiation case). In this case, the procedures mentioned in the crystallization mechanism (1)–(3) in Sec. III B 1 are the same, while procedures (4) and (5) are as follows.

(4) However, due to the lowering of the equilibrium wafer temperature, the diffusion coefficient of vacancies decreases, whereas the number of knocked-on interstitial Si atoms from the amorphous layer is constant. The number of knocked-on interstitial Si atoms does not depend on the substrate temperature, but is only determined by the incident energy and ion species (mass). Therefore, the number of interstitial Si atoms supplied from the amorphous layer becomes larger than that of the vacancies supplied from the crystalline substrate, as shown in Fig. 12(b).

(5) After vacancies and interstitial Si atoms are combined at the crystalline-amorphous interface, the interstitial atoms are left. This is clearly shown in Fig. 12(b), as the solid arrows are larger than those for open arrows at the interface. This means that the amorphous layer thickness is enlarged, that is, layer-by-layer amorphization occurs at the interface.

Assuming that the supply rate of vacancies from the crystalline substrate to the amorphous layer is V, V should be proportional to the vacancy diffusion coefficient and represented to be $V = V_0 \exp(-\Delta\mathcal{E}/kT)$. Here, $\Delta\mathcal{E}$ is an activation energy of vacancy migration (thermal diffusion) in the crystalline Si substrate, and V_0

can be the function of incident ion energy E and ion mass M, as $V_0(E,M)$. It can also be assumed that the supply rate of Si interstitial atoms from the amorphous layer (knocked-on atoms) does not depend on the equilibrium substrate temperature, but is only determined by the incident ion energy and mass. That is, the supply rate of knocked-on Si atoms from the amorphous layer to the crystalline substrate can be written as $V_1 = V_1(E,M)$. Therefore, the total (or net) crystallization rate or amorphization rate V_{tot} can be written as follows:

$$V_{tot} = V_0(E,M)\exp(-\Delta\mathcal{E}/kT) - V_1(E,M) . \quad (6)$$

V_0 and V_1 can be represented as a function of E and M as a general principle, but in this section these functions are used only as fitting parameters.

By fitting Eq. (6) with experimental results of the substrate temperature dependence on the recrystallized thickness shown in Fig. 4(b), the activation energy for vacancy migration was obtained as $\Delta\mathcal{E} = 0.1$ eV. This is shown by the dashed line in Fig. 15. Correctly speaking, the substrate temperature dependence on the crystallized thickness shown in Fig. 4(b) should not be represented by a straight line but by a curved line which is saturated at the lower temperature range.

It has already been clarified[22] that crystallization of the cylindrical damaged region in the crystalline Si substrate around the incident ion tracks occurred with the low activation energy of 0.18 eV. It was predicted that this low activation energy was attributed to the migration of doubly negative vacancies due to the same activation energy value proposed by Watkins.[20] The above-obtained low activation energy of 0.1 eV for crystallization of the amorphous Si layer on the crystalline Si substrate by high-energy heavy-ion beam irradiation also strongly suggests that these recrystallization processes are ruled by the doubly negative vacancy migration mechanism, as has been detailed in this paper.

By introducing minus velocity $-V_1$, both crystallization and amorphization can be explained comprehensively. The fitting parameters $V_0(E,M)$ and $V_1(E,M)$ are 7500 Å/(5.0×10^{15}/cm^2) and 420 Å/(5.0×10^{15}/cm^2), respectively.

Here, it is speculated why amorphization occurs first at the crystalline-amorphous interface, rather than at the projected range (R_p) of $^{75}As^+$ ions, where the ENDED is larger than at the interface. Whereas the crystallization of the amorphous Si layer on the crystalline Si substrate is attributed to the vacancy diffusion parallel to the incident ion tracks, the crystallization of the damaged regions in the crystalline Si substrate formed by irradiation ions themselves at the near R_p (1–2 μm depth) can be explained by radial vacancy migration in the cylindrical damaged volume, and by recombination with interstitial atoms already residing there. When the substrate temperature is lowered, diffusion coefficients both in the vertical and parallel directions decrease; however, *the diffusion coefficient in the vertical direction might originally be larger than that in the parallel direction,* as shown in Fig. 12(a). Therefore, even if both diffusion coefficients are diminished by lowering the substrate temperature, and if the supply of knocked-on Si atoms becomes comparatively larger than that of vacancies at the crystalline-amorphous interface, crystallization at the near R_p still occurs due to the originally larger diffusion coefficient, as shown in Fig. 12(b). That is, although produced vacancy and interstitial concentrations are larger at the near R_p than at the interface due to the large ENDED, crystallization in the near R_p occurs more effectively than at the interface.

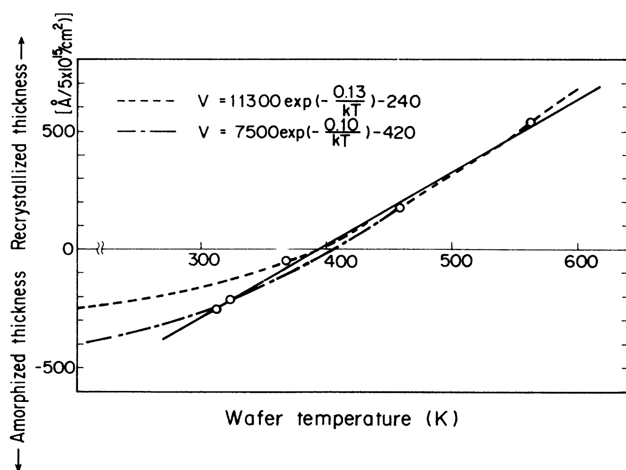

FIG. 15. The amorphization or recrystallization rate dependence on the substrate temperature during irradiation. The circles were experimentally measured values. The dashed line was deduced from a semiempirical equation, considering the balance between the vacancy supply and the knocked-on interstitial Si atom supply.

D. Comparison with other author's results

In this section the experimental results of Sec. II will be compared with other published results. Additionally, the influence of the ENDED and IEDED ratio on the recrystallized thickness of amorphous Si layers on the crystalline Si substrates is discussed.

Figure 16 shows the ENDED dependence of incident $^{20}Ne^+$ ions on the recrystallized thickness of amorphous Si layers on the crystalline Si substrates obtained by Williams *et al.*[7] In this figure the horizontal axis denotes S_n, which is the ENDED per one incident ion. The vertical axis represents the recrystallized thickness of amorphous Si layers on the crystalline Si substrates. The solid lines show the same substrate temperature and dashed lines represent the same incident ion energy. As clearly seen from this figure, the recrystallized thicknesses increase with the increase in the substrate temperatures from 200 °C to 400 °C and decrease with the increase in irradiation energy from 0.6 to 3.0 MeV. That is, the recrystallization rate decreases with the increase in incident ion energy. From a different point of view, Fig. 16 shows that the recrystallization rate increases as S_n increases. That is, as the number of vacancies and interstitials produced in the crystalline Si substrate under the amorphous Si

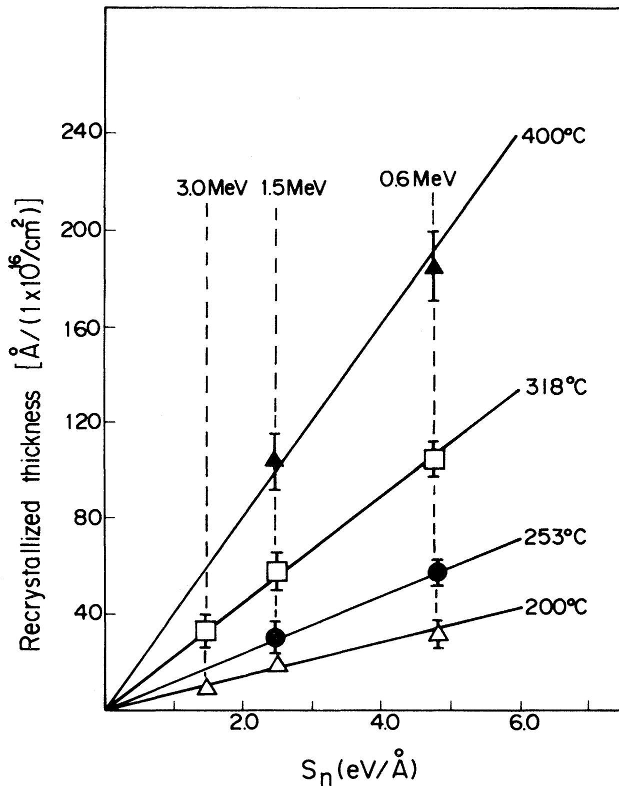

FIG. 16. The nuclear deposited energy density dependence on the recrystallized thickness by $^{20}Ne^{+}$ irradiation for various irradiation energy and the substrate temperatures reported by Williams *et al.* (Ref. 7).

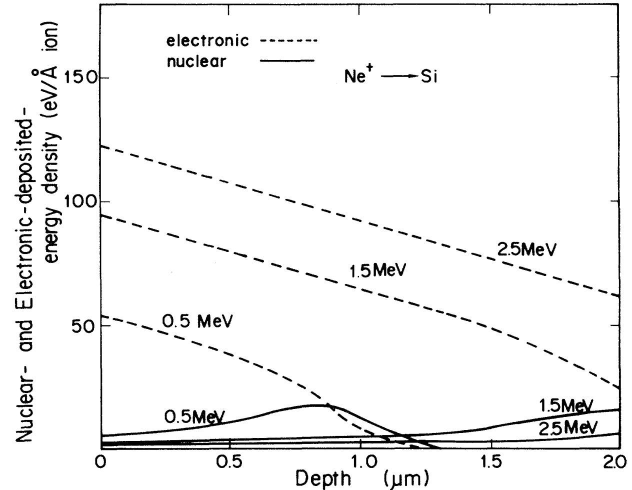

FIG. 17. The nuclear (solid lines) and electronic (dashed lines) deposited energy density distributions of $^{20}Ne^{+}$ ions in Si for various irradiation energy.

layer becomes large, the crystallization rate increases. However, these results contrast strongly with those of the author's on irradiation energy dependence. In the author's $^{75}As^{+}$ irradiation case, the recrystallized thickness increases with the increase in irradiation energy [see Figs. 6(a) and 6(b)].

The S_n in the $^{20}Ne^{+}$ irradiation case decreases with the increase in incident ion energy, because the nuclear scattering cross sections decrease with the increase in irradiation energy. This tendency also applies in the $^{75}As^{+}$ irradiation case. Nevertheless, the energy dependences are quite contrary. In the following, the author speculates on these differences in incident ion energy dependences between light $^{20}Ne^{+}$ ions and heavy $^{75}As^{+}$ ions.

The number of vacancies and interstitial atoms produced in the crystalline substrate is proportional to the ENDED of incident ions, and the number of electron-hole pairs is proportional to the IEDED. Therefore, in considering the difference between the $^{75}As^{+}$ and $^{20}Ne^{+}$ irradiation cases, it is necessary to calculate the ENDED and IEDED distributions in Si for $^{20}Ne^{+}$ ions, as is done in the $^{75}As^{+}$ irradiation case shown in Figs. 13(a) and 13(b).

Figure 17 shows the ENDED and IEDED distributions[21] in the Si substrate for $^{20}Ne^{+}$ ions. Comparing this figure with Figs. 13(a) and 13(b), it is clear that the ENDED for $^{20}Ne^{+}$ ions are one order of magnitude smaller than those for $^{75}As^{+}$ ions, whereas the IEDED are comparable to those of $^{75}As^{+}$. These calculations are based on the Lindhard-Scharff-Schiött (LSS) theory. The ENDED distributions in Fig. 17 mean that $^{20}Ne^{+}$ ions penetrate deeply in the crystalline Si substrate with low probability for colliding with Si substrate atoms at the crystalline-amorphous interface.

Figure 18 shows the ENDED and the IEDED chart for various ion species and irradiation energies. The horizontal and vertical axes represent the ENDED and the IEDED at the crystalline-amorphous interface (~ 1150 Å from the surface), respectively. Here, $^{75}As^{+}$ ions are denoted by open squares and $^{20}Ne^{+}$ ions are represented by solid circles. As also clearly seen in this figure, the ENDED for $^{20}Ne^{+}$ ions are one order of magnitude smaller than those for $^{75}As^{+}$ ions, whereas the IEDED is comparable to those for $^{20}Ne^{+}$ ions. Therefore, from Figs. 17 and 18, it can be said that the number of vacancies and interstitials for $^{20}Ne^{+}$ irradiation is one order of magnitude smaller than that for $^{75}As^{+}$, whereas the number of electron-hole pairs is comparable for both $^{20}Ne^{+}$ and $^{75}As^{+}$. These facts are the essence of the differences between the energy dependence on the recrystallized thickness for $^{20}Ne^{+}$ and $^{75}As^{+}$ ions. The reason for the difference between $^{20}Ne^{+}$ and $^{75}As^{+}$ ions is thoroughly explained in detail in Secs. III D 1 and III D 2.

1. *Energy dependence for $^{20}Ne^{+}$ ion irradiation*

Although the total ENDED integrated to the depth direction becomes small as the irradiation energy decreases, the ENDED at the crystalline-amorphous interface increases inversely, as shown in Figs. 13(a) and 17. Therefore, the number of vacancies and interstitial Si atoms at the crystalline-amorphous interface, which directly contribute to the crystallization of the amorphous Si layer, increases when the irradiation energy de-

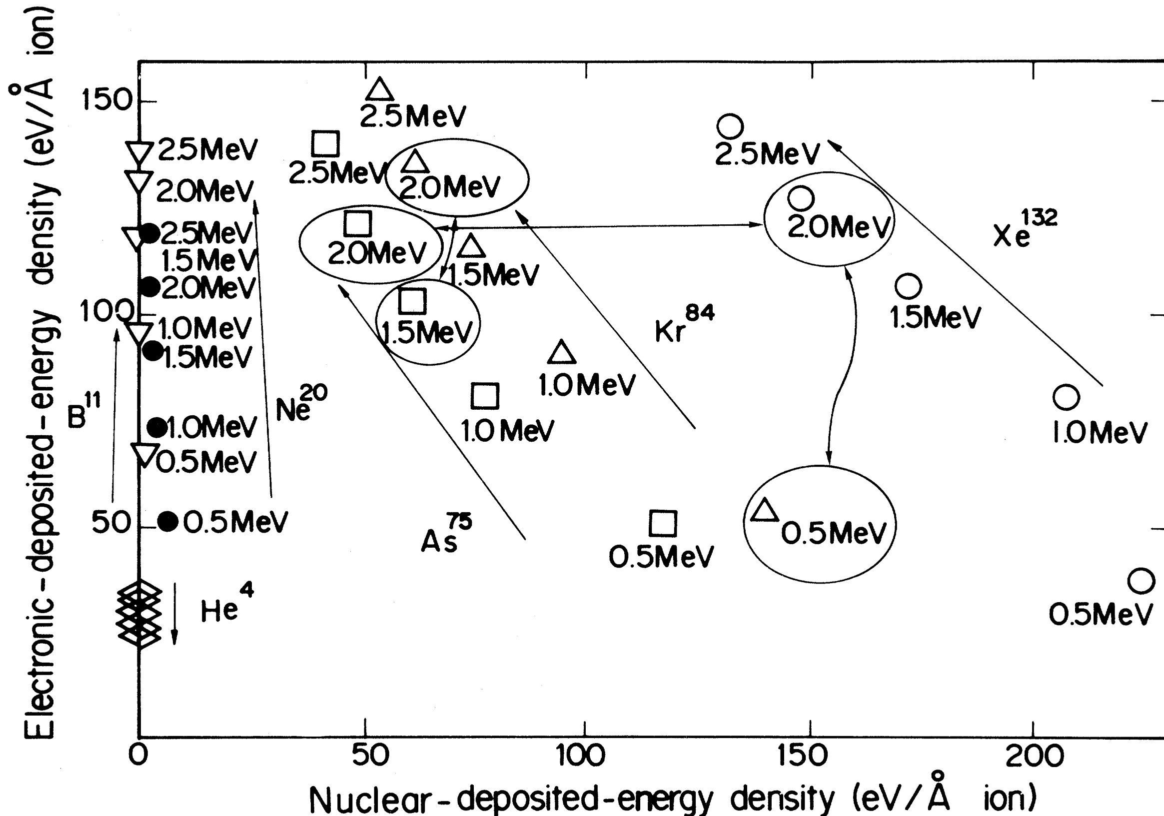

FIG. 18. The nuclear and electronic deposited energy densities at the crystalline-amorphous interface for various irradiation energy and ion species.

creases. Although the number of electron-hole pairs decreases as the irradiation energy is lowered, *the number of doubly negative vacancies might be saturated from the beginning,* because the produced vacancies and interstitials are originally one order of magnitude smaller than those produced by $^{75}As^{+}$ ions. Therefore, although the number of electron-hole pairs decreases when the irradiation energy is lowered, the number of doubly negative vacancies might increase. This is the reason the recrystallization rate increases as the irradiation energy decreases for $^{20}Ne^{+}$ light-ion irradiation.

2. *Energy dependence for $^{75}As^{+}$ irradiation*

The number of vacancies and interstitial Si atoms at the crystalline-amorphous interface increases when the irradiation energy is lowered, the same as in the $^{20}Ne^{+}$ irradiation case. However, produced vacancies and interstitial Si atoms are originally one order of magnitude greater than for $^{20}Ne^{+}$ irradiation, and *the doubly negative vacancies might not be saturated from the beginning.* Therefore, although the number of vacancies increases as the irradiation energy is lowered, the doubly negative vacancies decrease inversely as a result of decreasing the number of electron-hole pairs. This is why the recrystallization rate increases as the irradiation energy increases for $^{75}As^{+}$ heavy-ion irradiation.

Thus, the author predicts that the energy dependence on the crystallized thickness becomes more remarkable as the irradiation ion mass increases. In order to understand the influence of the ENDED and the IEDED on the crystallization rate more precisely and directly, one may vary the IEDED under the same ENDED conditions. For example, one can directly ascertain the role of IEDED in the crystallization processes of amorphous Si layers, if the recrystallization rate is enhanced by irradiating electrons, ultraviolet lights, or x rays simultaneously during ion beam irradiation.

IV. APPLICATIONS AND ISSUES TO BE SOLVED HEREAFTER

In this last section applications are discussed, particularly upon the formation of the SOI structure. The recrystallization of amorphous Si layers by high-energy heavy-ion beam irradiation is strongly characterized by low-temperature ($\leq 300\,°C$) processes far below the normal SPEG temperature of $\sim 600\,°C$. In order to utilize this low-temperature characteristic and the resulting characteristics of low thermal stress, high-energy heavy-ion beam irradiation is suitable for the formation of the

SOI structure and for the activation of dopant atoms in the GaAs substrates that requires a low annealing temperature.

A. Applications

1. Formation of the SOI structure

Figure 19 shows a cross-sectional view of the SOI structure. The ~10-μm-width SiO_2 stripe layers of ~1000 Å thicknesses were formed on the crystalline Si substrate. Thereafter, the CVD amorphous Si layer of ~4000 Å thickness was deposited on both the stripe SiO_2 layers and on the crystalline Si substrate. After deposition, the samples were annealed at ~600 °C for 24 hours. Figure 20(a) shows the reflection high-energy electron-diffraction (RHEED) pattern of this furnace-annealed sample.[23] Because only partial areas of the amorphous Si layer that were in contact with the crystalline Si substrate through the narrow window surrounded by the amorphous SiO_2 film crystallized by furnace annealing, and because this crystallization did not proceed laterally onto the SiO_2 film, the characteristic halo pattern of amorphous Si was clearly observed.

After annealing for 24 hours at 600 °C, the furnace-annealed sample was irradiated by 2.5-MeV $^{75}As^{+}$ ions for a $1.0\times10^{16}/cm^2$ dose with a ~3.5 $\mu A/4\ cm^2$ dose rate. This dose rate resulted in a ~300 °C substrate temperature.

Figure 20(b) shows the RHEED pattern of this high-energy heavy-ion beam irradiated sample.[23] The halo pattern disappeared and crystallization proceeded laterally onto the ~10-μm-width SiO_2 film, although the crystallinity was not very fine. It should be remembered that the crystallization rate of the CVD amorphous Si layer on the crystalline Si substrate, that is, the crystallization rate in the vertical direction (layer-by-layer crystallization rate), was only ~60 Å/($1.0\times10^{15}/cm^2$), as shown in Fig. 8. Therefore, the vertical crystallized thickness ought to be at most ~600 Å with a $1.0\times10^{16}/cm^2$ dose. However, the crystallization proceeded laterally onto the SiO_2 film even of the ~10 μm length.

Here, the crystallized area of the amorphous Si layer on the crystalline Si substrate is the irradiated area itself, if the SiO_2 film is withdrawn. Assuming that the diameters of the initially formed cylindrical damaged regions (recrystallized by vacancy migration and recombination mechanisms, as mentioned before) around the incident ion tracks are ~50 Å, the doses needed for those damaged areas to overlap the entire irradiated area are $1.0\times10^{12}/cm^2$–$1.0\times10^{13}/cm^2$. Therefore, the doses

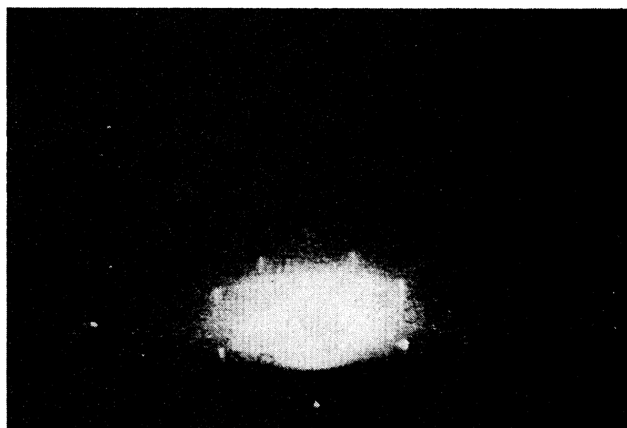

(a)

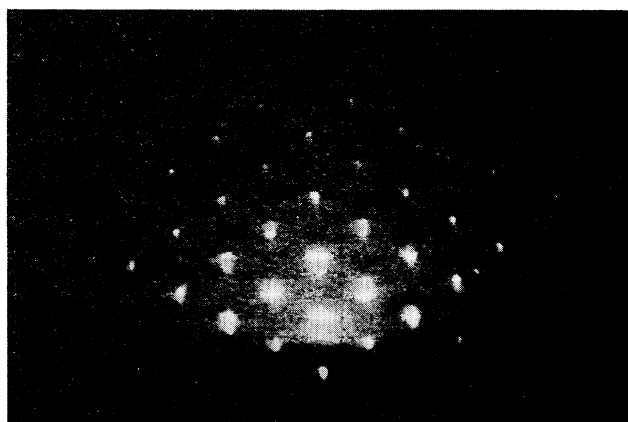

(b)

FIG. 20. (a) The RHEED pattern of the SOI structure after annealing for 24 hours at 600 °C. The characteristic halo pattern was observed. (b) The RHEED pattern by 2.56-MeV $^{75}As^{+}$ ion irradiation after furnace annealing for 24 hours at 600 °C for a $1.0\times10^{16}/cm^2$ dose with a 3.5 $\mu A/4\ cm^2$ dose rate which resulted in the ~300 °C substrate temperature. The halo pattern disappeared and crystallization proceeded onto the 10-μm-width SiO_2 film.

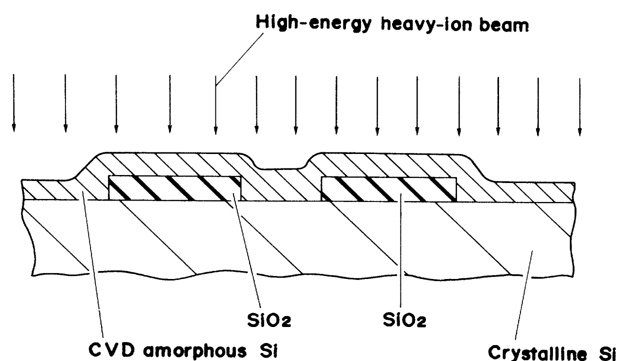

FIG. 19. The cross-sectional view of the SOI structure. The CVD amorphous Si layer was deposited on the patterned SiO_2 film and on the bare crystalline Si substrate between the SiO_2 film. First, the samples were furnace annealed and the amorphous layer crystallized vertically on the crystalline Si substrate; however, crystallization did not proceed laterally onto the SiO_2 film. Then a high-energy heavy-ion beam was irradiated and the amorphous layer crystallized laterally onto the SiO_2 film.

$1.0\times10^{15}/\text{cm}^2-1.0\times10^{16}/\text{cm}^2$ in the present irradiation conditions are enough for crystallizing the entire irradiated area.

Taking into consideration the vacancy diffusion in the radial (lateral) direction of the cylindrical damaged volumes around the incident ion tracks at a low temperature with low thermal stress, it might be possible that the crystallization proceeded onto the wide areas of the amorphous insulator in such SOI structures.

Recently, Voelskow *et al.*[24] succeeded in formation of the SOI structure using a 330-keV $^{28}Si^+$ ion beam; however, the lateral spread of crystallization was only ~1.5 μm. The irradiation conditions such as beam energy, the substrate temperatures, etc., must be thoroughly taken into account.

2. The GaAs compound semiconductor annealing

The compound semiconductors such as GaAs become electrically positive or negative by replacing the Ga or As lattice sites with Si atoms doped, for example, by ion implantation. In order to obtain a high activation efficiency, high-temperature annealing is needed. However, As atoms, a main constituent of a GaAs substrate, have a disposition for evaporating from the surface in the high-temperature circumstances. Therefore, various annealing methods, such as cap annealing, have been considered.

If this low-temperature ion-beam annealing is successfully applied, the process is simplified. Moreover, using As atoms as irradiation species, there will be no unfavorable influence on the GaAs substrate, for As atoms are the constituents of GaAs substrates. These trials have already been undertaken and good results have been obtained.[25]

B. Issues to be solved hereafter

The mechanism of ion-beam-induced low-temperature crystallization of the amorphous Si layers on the crystalline Si substrates has been speculated on and clarified; however, there still exist several issues to be solved. In this section these problems are discussed and new phenomena found in continuing experiments are shown.

1. The dose-rate dependence of recrystallized thickness for various irradiation energies

Figure 21(a) shows the ⟨100⟩-channeling spectra of high-energy heavy-ion beam irradiated samples for various incident energies in order to investigate the energy dependence on the recrystallized thickness. The substrate temperature had been kept at the constant value of ~195 °C by varying the beam currents (dose rate) to produce the same input power density. The irradiated doses were $5.0\times10^{15}/\text{cm}^2$, using a 4-cm^2 area mask.

As clearly seen from this figure, the recrystallization rate was the highest for 2.56-MeV irradiation. For the 2.00- and 1.56-MeV cases, the recrystallized thicknesses were almost the same and were smaller than that of the 2.56-MeV case. The amorphous layer thickness was enlarged, that is, layer-by-layer amorphization occurred in the 1.03-MeV case, as in the case of low-temperature (≤120 °C) irradiation with 2.56 MeV energy. Whereas the layer-by-layer amorphization occurred below the ~120 °C substrate temperature at 2.56 MeV, the same phenomenon occurred at the higher temperature of ~195 °C at 1.03 MeV. Therefore, the threshold temperature for amorphization and crystallization increases as the irradiation energy decreases. In other words, the recrystallization phenomenon becomes remarkable as the irradiation energy increases at the same substrate temperature. These experimental results of 1.54–2.56-MeV energy dependence on the recrystallized thickness shown in Fig. 21(a) coincided with the results in Sec. II F obtained with a large scanning area of 62 cm^2, shown in Fig. 6(a).

However, drawing attention to the deeper region in the crystalline Si substrate, the buried amorphous layer was found in the 1.03-MeV case. In Fig. 21(a), the SSB detector was settled at a 110° angle to the probe He beam direction in order to improve the depth resolution. The surface amorphous Si layer region was the only region of interest.

In Fig. 21(b), the ⟨100⟩-channeling spectra of the same samples as in Fig. 21(a) are shown. They were obtained by setting the SSB detector at a 170° angle to see the deeper region. As clearly seen from this figure, not only for the 1.03-MeV case but also for the 1.54-MeV irradiation, buried amorphous layers were formed in the depth near the R_p of incident $^{75}As^+$ ions, due to the nuclear scattering of the high-energy $^{75}As^+$ ion beam.

It was reported previously[22] that the damages induced in the crystalline Si substrate by high-energy heavy-ion beam irradiation were much smaller than those predicted by the ENDED estimation or those induced by low-energy (several tens of kilo-electron volts) ion implantation, even if the annealing effects during irradiation were taken into account. Figure 22 shows the ⟨111⟩-channeling spectra of 1.54-MeV $^{75}As^+$ ion irradiated (111) crystalline samples for various doses with a dose rate of 3.0 μA/40 cm^2. The damage increases with an increase in dose. However, even if the dose reaches $5.0\times10^{15}/\text{cm}^2$ (open triangles), the damage degree remains small. The substrate temperature had been kept at ~260 °C during irradiation, on this dose-rate condition.

On the other hand, in Fig. 21(b) for the same 1.54 MeV energy and the same $5.0\times10^{15}/\text{cm}^2$ dose with the different 1.77 μA/4 cm^2 dose-rate (open circles) irradiation, the buried amorphous layer was formed by the irradiation beam itself, although the ~195 °C substrate temperature was lower than ~260 °C in Fig. 22. In Ref. 22 the author introduced damage degree at R_p or $D_d(R_p)$ as

$$D_d(R_p)=[Y_d(R_p)-Y_0(R_p)]/[Y_r(R_p)-Y_0(R_p)] , \quad (7)$$

where $Y_d(R_p)$ and $Y_0(R_p)$ are the yields at R_p of ⟨111⟩-channeling spectra for a high-energy $^{75}As^+$ ion irradiated sample and an unirradiated bulk crystalline sample, respectively. $Y_r(R_p)$ is the yield at R_p of the normal RBS spectrum in the random direction.

Figure 23 shows the damage degree at R_p versus the substrate temperature during irradiation with a $1.0\times10^{15}/\text{cm}^2$ dose for various irradiation energies and

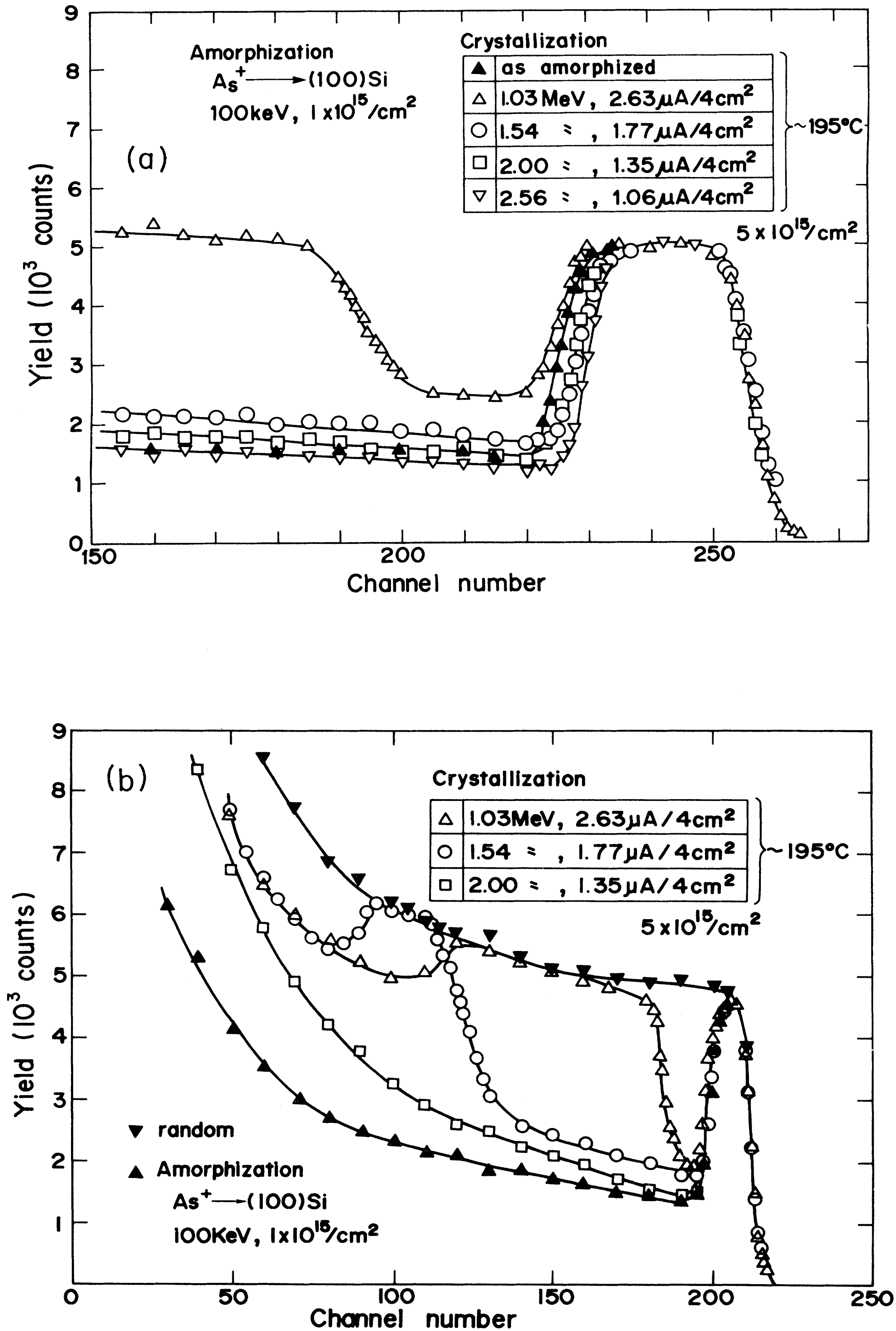

FIG. 21. (a) ⟨100⟩-channeling spectra of (100) Si after crystallization by $^{75}As^+$ ion irradiation for a $5.0\times10^{15}/cm^2$ dose with various irradiation energy. The dose rates were varied from 1.06 $\mu A/4\ cm^2$ to 2.63 $\mu A/4\ cm^2$ so that the substrate temperatures might be the same value of $\sim 195\,^{\circ}C$ for different irradiation energy. The SSB detector was settled at a 110° angle to the probe He beam direction to improve the depth resolution. (b) The same ⟨100⟩-channeling spectra as in (a); however, the SSB detector was settled at a 170° angle to observe deep in the crystalline Si substrate.

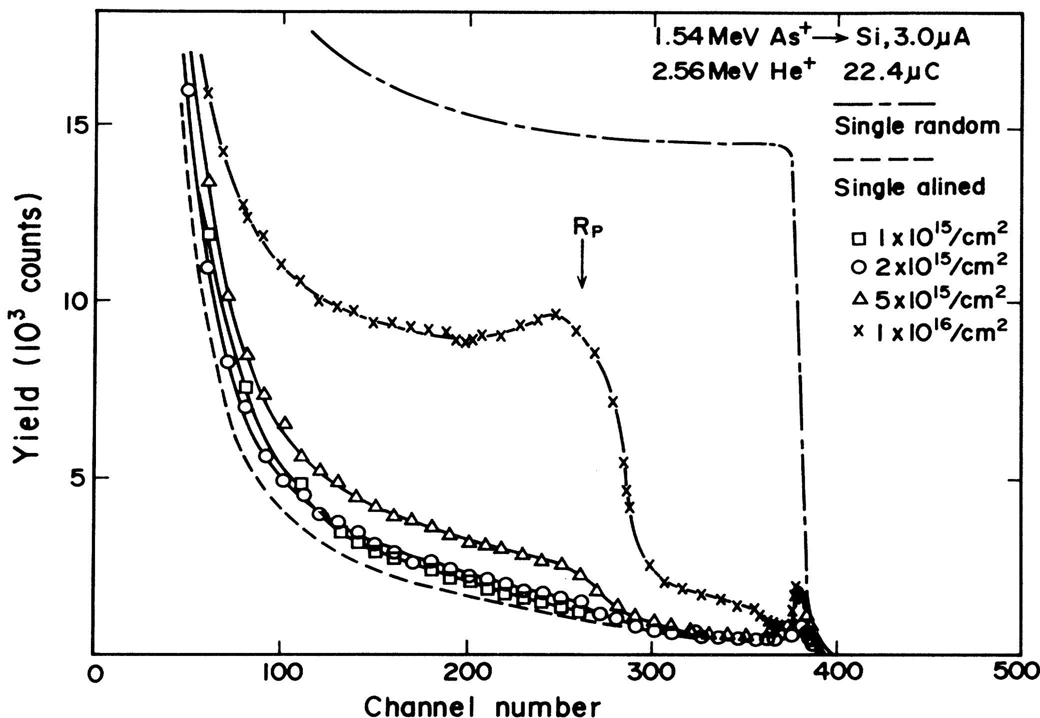

FIG. 22. ⟨111⟩-channeling spectra of the (111) bulk crystalline Si after irradiation by 1.54 MeV $^{75}As^+$ ions for various doses with a 3.0 μA/40 cm^2 dose rate. The probe He beam energy was 2.56 MeV.

dose rates. It was speculated[22] that the crystallization of cylindrical damaged volumes in the crystalline substrate around the incident ion tracks occurred by the vacancy migration (thermal-diffusion) mechanism. From the slope in Fig. 23, the activation energy for vacancy migration was deduced as 0.18 eV, which coincided with the activation energy of 0.18 eV for doubly negative vacancy migration proposed by Watkins.[20]

From Fig. 23, in the case of 1.03- and 1.54-MeV energies with a 5.0×10^{15}/cm^2 dose at the $\sim$195 °C substrate temperature, $D_d(R_p)$ is expected to be 0.1–0.2, whereas the buried amorphous layers were formed in Fig. 21 for both 1.03 and 1.54 MeV cases, in spite of the same substrate temperatures, irradiation energies, and doses. Thus, the effective annealing in the crystalline Si substrate during high-energy heavy-ion beam irradiation that the author reported previously[22] does not seem to occur under these Fig. 21 experimental conditions. The only different irradiation conditions in Fig. 21 compared with Figs. 22 or 23 were the dose rates. That is, in Fig. 21, the samples were irradiated through a 4-cm^2 area mask to shorten the irradiation period.

Therefore, at first, it seemed that those differences between the damage degree in the crystalline Si substrate shown in Figs. 21 and 22 (or Fig. 23) were attributed to the dose-rate differences. That is, in Fig. 23 (40-cm^2 scanning area), the dose rates of $\sim$1.6 μA/40 cm^2 for 1.54 MeV and $\sim$2.4 μA/40 cm^2 for 1.03 MeV were needed to produce the $\sim$195 °C substrate temperature. However, in Fig. 21 (4-cm^2 scanning area), about one-order-of-magnitude-higher dose rates of $\sim$1.77 μA/4 cm^2 for 1.54 MeV and $\sim$2.63 μA/4 cm^2 for 1.03 MeV were needed to produce the same $\sim$195 °C substrate temperature, due to the cooling effect of partial irradiation. The buried amorphous layers shown in Fig. 21(b) seemed to be formed by this one-order-of-magnitude-higher dose rate.

In conclusion, the buried amorphous layers were only formed when the samples were irradiated below $\sim$1.5 MeV energy and through a 4-cm^2 area mask. Thus, the influence of the dose rate on the experimental results in Sec. II can be overlooked, because in almost all results, such as dose dependence, dose-rate dependence, substrate temperature dependence, etc., except for the energy dependence, the irradiation energies were 2.56 MeV.

Only the energy-dependence results obtained by using a 4-cm^2 area mask shown in Fig. 21(a) might not show the precise energy dependence on the recrystallized thickness, even if the substrate temperature had been kept at the constant value of $\sim$195 °C. Therefore, the author tried again to examine accurately the energy dependence by irradiating a wider scanning area of 62 cm^2 to obtain lower dose rates than for a 4-cm^2 scanning-area case. The experimental results in Sec. II F showing the energy dependence on the recrystallized thickness were thus obtained, and eventually the results shown in Figs. 6(a) and 21(a) were almost the same.

In order to investigate the damage formation in the crystalline Si substrate at "low energy" below $\sim$1.5 MeV

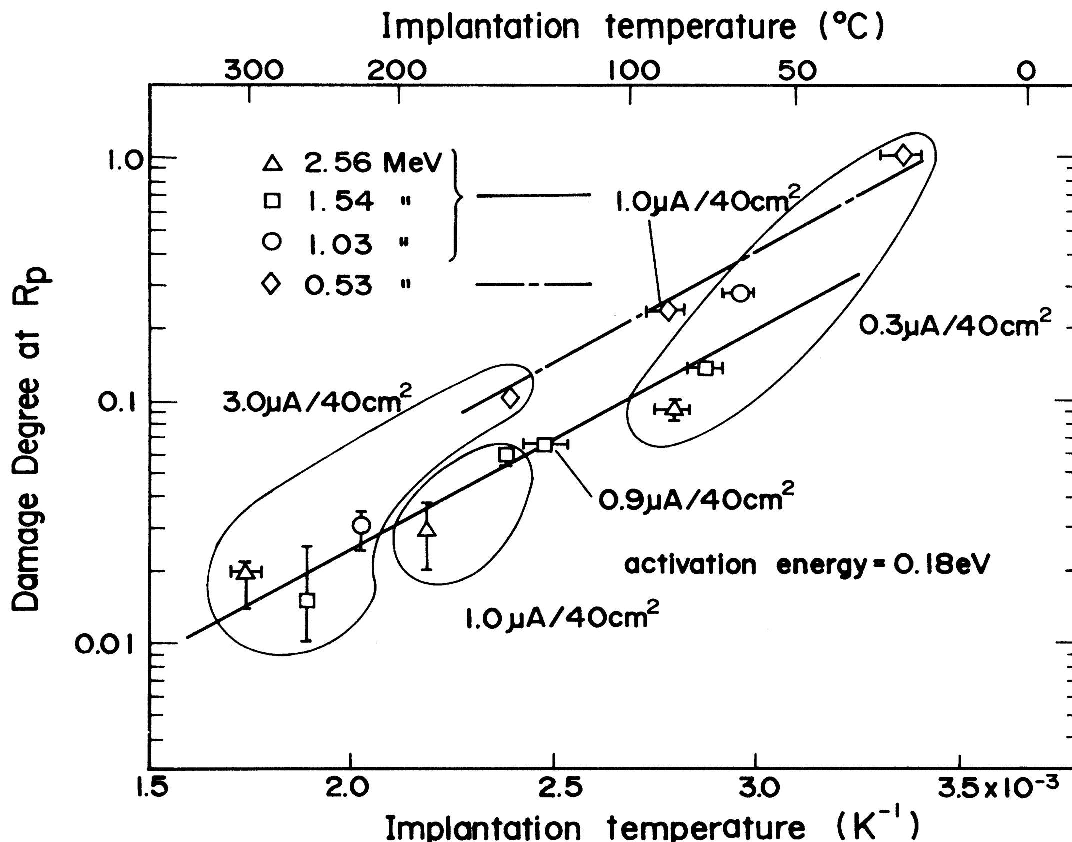

FIG. 23. Damage degree at R_p dependence on the substrate temperature during irradiation for various irradiation energy and dose rates with a $1.0\times10^{15}/cm^2$ dose.

under the high-dose-rate (4-cm^2 scanning-area) condition, the author thoroughly examined the damage degree for various doses.

2. *The damage degree in the crystalline substrate for various doses under high dose rate*

As mentioned in Sec. IV B 1, damages were substantially introduced in the crystalline Si substrate below ~ 1.5 MeV irradiation energy and with a high dose rate using a 4-cm^2 area mask. Figure 24 shows the $\langle 111 \rangle$-channeling spectra of a 1.03-MeV energy irradiated (111) crystalline Si sample with a 2.6 μA/4 cm^2 dose rate for various doses. This irradiation energy and dose rate resulted in the $\sim 195\,^\circ$C equilibrium substrate temperature, measured by heat labels attached to the back side of wafers. As clearly seen from this figure, damages were introduced considerably for a $1.0\times10^{14}/cm^2$ dose. The amorphous layers were thoroughly grown from deep in the substrate to the near surface for the $5.0\times10^{14}/cm^2$ dose. Then the thick amorphous layer crystallizes both from the surface and from deep inside with further increases in irradiation doses.

It is to be noted that the $D_d(R_p)$ was only ~ 0.03 for the $1.0\times10^{15}/cm^2$ dose at the $\sim 195\,^\circ$C substrate temperature from Fig. 23 for 40-cm^2 scanning-area cases. Thus, it seems that the damage annealing processes during high-energy heavy-ion beam irradiation, discussed in Ref. 22, does not occur with the high dose rate of the 4-cm^2 scanning-area case.

However, considering further, there is another point of view. That is, under the present experimental conditions, the Si wafers were heated up by the high-energy ion beam itself. So, as calculated in Sec. III A, the Si wafer temperatures had been kept at temperatures lower than the equilibrium values in the initial stage of irradiation. In the case for the 2.6 μA/4 cm^2 dose rate shown in Fig. 24, it takes only ~ 25 sec to reach the $1.0\times10^{14}/cm^2$ dose. The transient wafer temperature after the $1.0\times10^{14}/cm^2$ dose irradiation, that is, the substrate temperature at ~ 25 sec, is at most $\sim 70\,^\circ$C, far below the equilibrium temperature of $\sim 195\,^\circ$C. Thus, a considerable amount of damages was certainly introduced at such a low temperature. The wafer temperature reaches equilibrium values for the $\sim 5.0\times10^{15}/cm^2$ dose and the continuing irradiation of the high-energy beam induces recrystallization of the buried amorphous layer formed in the initial stage of irradiation according to the vacancy migration mechanism minutely discussed and speculated on in Sec. III B.

In Fig. 24 the buried amorphous layer was recrystallized both from the surface and from deep in the crystalline substrate. If the crystalline nucleations are left near the surface, recrystallization should naturally occur by the vacancy migration mechanism, that is, vacancies are

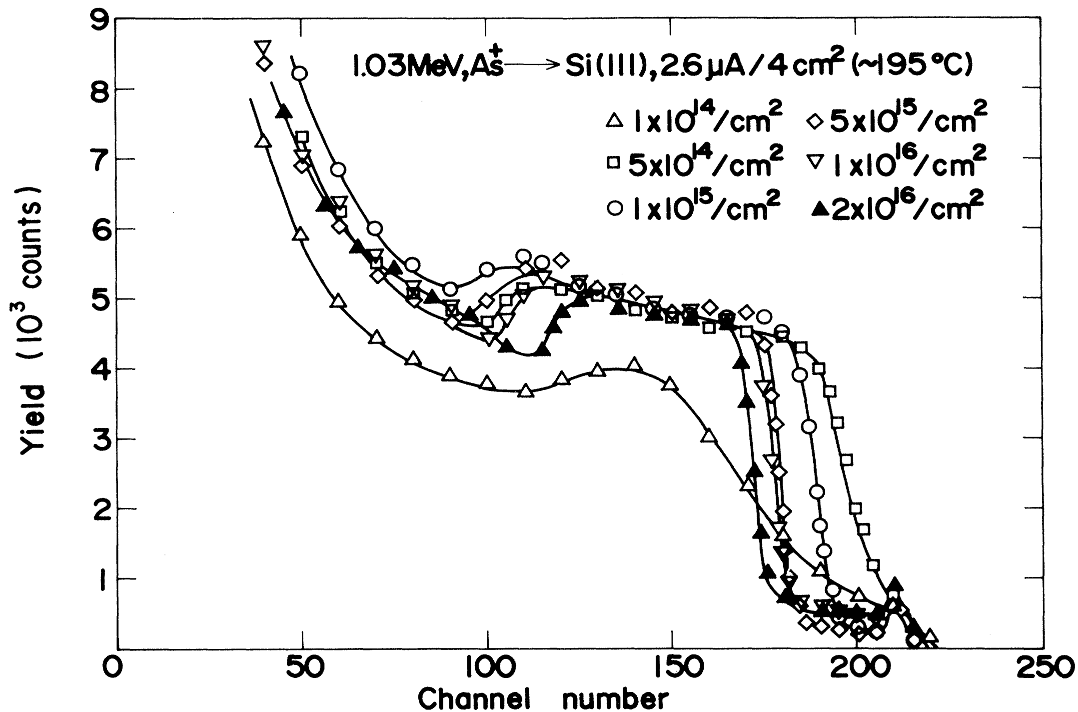

FIG. 24. ⟨111⟩-channeling spectra of the (111) bulk crystalline Si after irradiation by 1.03-MeV $^{75}As^+$ ions for various doses with a 3.0 $\mu A/4\ cm^2$ dose rate.

supplied not only from deep in the crystalline substrate but also from the surface crystalline region to the buried amorphous layer.

In conclusion, to solve the issues mentioned in Secs. IV B 1 and IV B 2, that is, to clarify whether the cause of the considerable amount of damage observed below the ~ 1.5-MeV irradiation energy with a 4-cm^2 scanning-area mask lies in the dose-rate effect itself or in the transient substrate temperature during irradiation, the wafer holder must be equipped with the heater to warm up the wafers and must have been kept under the same temperature regardless of different dose rates.

3. The role of inelastic electronic scattering in the vacancy migration process

It was discussed in Sec. III B that the crystallization of amorphous Si layers on the crystalline Si substrates occurred at a low temperature far below the normal SPEG temperature by supplying vacancies to the amorphous layer. The author speculated that the charge converting process from neutral to doubly negative vacancies by inelastic electronic scattering of the incident high-energy beam also contributed to enhance the crystallization rate. In order to directly ascertain this conversion process, the ultraviolet light, x rays, or electron beams with an appropriate energy and intensity should be irradiated simultaneously with the ion beam. If the crystallization rate is enhanced, the role of inelastic scattering is proved.

4. The layer-by-layer amorphization processes at low temperature

The author clarified the layer-by-layer amorphization mechanism at low temperature ($\leq 120\,^\circ$C in the 2.5-MeV $^{75}As^+$ ion irradiation case) and predicted that the amorphization thickness would be saturated as the substrate temperature was lowered. However, in order to understand the amorphization and damage formation mechanism thoroughly in detail, more data acquisition at low temperature—for example, at approximately the liquid nitrogen temperature—is needed.

V. CONCLUSIONS

The low-temperature crystallization phenomenon by ion beam irradiation was reviewed. Then the author minutely clarified and speculated on the mechanism of low-temperature crystallization and low-temperature layer-by-layer amorphization of amorphous Si layers on the crystalline Si substrates by high-energy heavy-ion beam irradiation. The vacancy migration model assisted by electron-hole pair production was proposed, which explained clearly and comprehensively both the crystallization and amorphization. Applications to forming the SOI structure by utilizing the low-temperature and low-thermal-stress characteristics, as well as issues to be solved in the future, were also referred to.

ACKNOWLEDGMENTS

I wish to express my sincere thanks to Dr. K. Komaki, Dr. S. Ino, Dr. K. Terakura, Dr. N. Nagasawa, and Dr. M. Tsukada of Tokyo University for critical discussions and suggestions. I am indebted to Dr. S. Yamamoto of Tokyo University, and my appreciation and thanks go to Dr. S. Furukawa and Dr. H. Ishiwara of the Tokyo Institute of Technology for their helpful discussions. I also wish to thank Dr. T. Suzuki and Dr. H. Mukai, M. Kondo, N. Oowada, H. Ikawa, and T. Sakai for their general encouragement, and Dr. K. Kajiyama for leading me to accomplish this work. I express my gratitude to Dr. T. Tsurushima and Dr. H. Tanoue for computing the nuclear and electronic deposited energy density distributions in Si of various ion species for various incident energies, and to Dr. Y. Kunii for TEM observations of the SOI structures. Lastly, I thank Y. Sakakibara and M. Takahashi for preparing the samples in these present experiments.

[1]M. Tamura, H. Tamura, and T. Tokuyama, Jpn. J. Appl. Phys. **19**, L23 (1980).

[2]H. Ishiwara, M. Nakano, H. Yamamoto, and S. Furukawa, Proceedings of the Fourteenth Conference on Solid State Devices, Tokyo, 1982 [Jpn. J. Appl. Phys. **22**, Suppl. 22-1, 607 (1983)].

[3]R. T. Hodgson, J. E. E. Baglin, R. Pal, J. M. Neri, and D. A. Hammer, Appl. Phys. Lett. **37**, 187 (1980).

[4]I. Golecki, G. E. Chapman, S. S. Lau, B. Y. Tsauer, and J. W. Mayer, Phys. Lett. **71A**, 267 (1979).

[5]J. Linnros, B. Svensson, and G. Holmen, Phys. Rev. B **30**, 3629 (1984).

[6]J. Linnros, G. Holmen, and B. Svensson, Phys. Rev. B **32**, 2770 (1985).

[7]J. S. Williams, R. G. Elliman, W. L. Brown, and T. E. Seidel, in *Layered Structures, Epitaxy, and Interfaces,* edited by J. M. Gibson and L. R. Dawson, MRS Symposia Proceedings No. 37 (Materials Research Society, Pittsburgh, 1985), p. 127.

[8]R. G. Elliman, J. S. Williams, S. T. Johnson, and E. Nygren, in *Beam-Solid Interactions and Transient Processes,* edited by M. O. Thompson, S. T. Picraux, and J. S. Williams, MRS Symposia Proceedings No. 74 (Materials Research Society, Pittsburgh, 1987), p. 471.

[9]J. Linnros, R. G. Elliman, and W. L. Brown, in *Beam-Solid Interactions and Transient Processes* (Ref. 8), p. 477.

[10]A. La. Ferla, E. Rimini, and G. Ferla, Appl. Phys. Lett. **52**, 712 (1988).

[11]J. Nakata and K. Kajiyama, Proceedings of the Thirteenth Conference on Solid State Devices, Tokyo, 1981 [Jpn. J. Appl. Phys. 21, Suppl. 21-1, 211 (1982)].

[12]J. Nakata and K. Kajiyama, Appl. Phys. Lett. **40**, 686 (1982).

[13]K. Kajiyama, J. Nakata, and M. Takahashi, Jpn. Appl. Phys. Soc. **52**, 2 (1983) (in Japanese).

[14]Y. Kunii, M. Tabe, and K. Kajiyama, Jpn. J. Appl. Phys. **21**, 1431 (1982).

[15]P. D. Party, J. Vac. Sci. Technol. **13**, 622 (1976).

[16]T. Takeda, A. Yoshii, and K. Wada, *1982 National Convention Record* (The Institute of Electronics and Communication Engineers of Japan, Tokyo, 1982), Part 2, p. 11 (in Japanese).

[17]D. A. Thompson and R. S. Walker, Radiat. Eff. **36**, 91 (1978).

[18]F. F. Morehead and B. L. Crowder, *Proceedings of the First International Conference on Ion Implantation, Thousand Oaks, California,* edited by L. T. Chaddelton and F. H. Eisen (Gordon and Breach, London, 1971), p. 25.

[19]L. Csepregi, E. F. Kennedy, J. W. Mayer, and T. W. Sigmon, J. Appl. Phys. **49**, 3906 (1978).

[20]G. D. Watkins, *Radiation Damage in Semiconductors* (Dunod, Paris, 1985), p. 97.

[21]T. Tsurushima and H. Tanoue, J. Phys. Soc. Jpn. **31**, 1695 (1971).

[22]J. Nakata, M. Takahashi, and K. Kajiyama, Jpn. J. Appl. Phys. **22**, 2211 (1981).

[23]J. Nakata and K. Kajiyama, Japanese Patent No. 1316930 (15 May 1986) (in Japanese).

[24]M. Voelskow, W. Skorupa, K. Wollschlaeger, J. Matthaei, P. Knothe, K.-H. Heinig, and H. Bartsch, Appl. Surf. Sci. **43**, 196 (1989).

[25]N. Kobayashi, in *Proceedings of the Thirteenth Symposium on Ion Sources and Ion-Assisted Technology, Tokyo, 1990,* edited by T. Takagi (The Ion Engineering Society of Japan, Tokyo, 1990), p. 357.

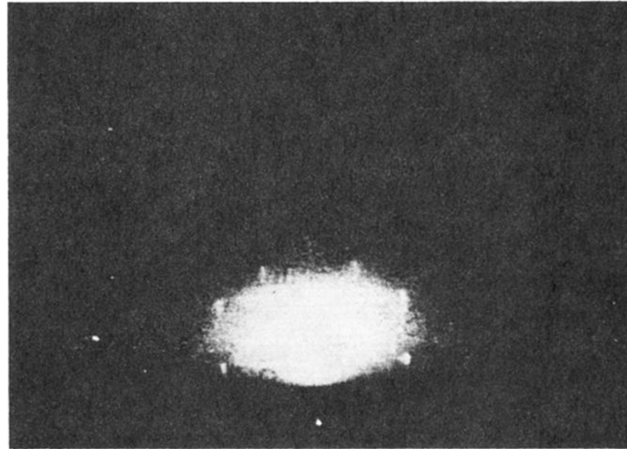

(a)

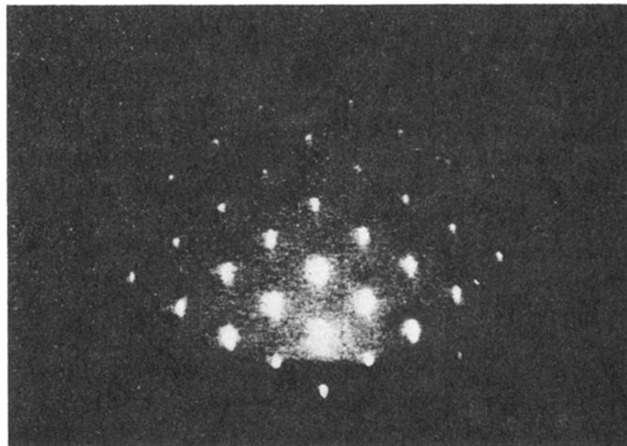

(b)

FIG. 20. (a) The RHEED pattern of the SOI structure after annealing for 24 hours at 600 °C. The characteristic halo pattern was observed. (b) The RHEED pattern by 2.56-MeV $^{75}As^+$ ion irradiation after furnace annealing for 24 hours at 600 °C for a $1.0\times10^{16}/cm^2$ dose with a 3.5 $\mu A/4\ cm^2$ dose rate which resulted in the ~300 °C substrate temperature. The halo pattern disappeared and crystallization proceeded onto the 10-μm-width SiO_2 film.